Master's Thesis

Crystal Structure and Luminescence Studies of Upconverting Nanoparticles

Gökhan Dumlupinar

A thesis submitted in fulfillment of the requirements
for the degree of Master of Science

in the

Biophotonics Group
Department of Physics

Lund University

April 2015

Thesis Supervisors: Prof. Stefan andersson-engels and Dr. Haichun liu

Abstract

Nanoparticles doped with lanthanide ions that are capable of upconverted radiation promise great potential as exogenous luminescent biomarkers in biomedical imaging. In this work, hexagonal structured core $NaYF_4$:Yb^{3+},Tm^{3+} and core-shell $NaYF_4$:Yb^{3+},Tm^{3+} @$NaYF_4$ upconverting nanoparticles (UCNPs) with ranging from ∼43 nm to ∼66 nm in size are successfully synthesized by a modified solvothermal synthesis method.

The work presented in this thesis aims at the crystal structure analysis of core $NaYF_4$:Yb^{3+},Tm^{3+} and core-shell $NaYF_4$:Yb^{3+},Tm^{3+}@$NaYF_4$ UCNPs under varying thermal conditions. X-ray diffraction (XRD) and transmission electron microscopy (TEM) techniques were utilized to characterize size, phase and shape of UCNPs. Moreover, thermal stability of the crystal phase of UCNPs was investigated. Thus, UCNPs were exposed to a post heating treatment where the temperature was gradually increased from room temperature to 700°C. The XRD patterns of UCNPs at varying temperature levels show that UCNPs are thermally stable up to ∼300°C. Additionally, at the temperature level of 590°C core UCNPs began to undergo a phase transformation from hexagonal phase (β) to cubic phase (α).

The low quantum yield (QY) of upconversion (UC) emissions in UCNPs is always considered as a challenging problem that hinders UCNPs' utilization in bioimaging. Therefore, another aim of this work is pointed to figure out a successful way that improves QY of core UCNPs. Indeed, a significant increase in QY of near infrared (NIR) UC emission in core-shell UCNPs was accomplished under the excitation of 975 nm light. Simulations promise that it is feasible to increase QY up to ∼2.4% by millisecond pulse excitation with carefully selected pulse parameters. Furthermore, NIR UC signal gain, ∼8.7, is experimentally achieved by the pulsed excitation that had a 2 Hz repetition rate, a 20 ms pulse width, a 4% duty cycle with ∼0.12 Wcm^{-2} average power density.

Acknowledgements

First of all, I would like to thank my supervisors, Prof. Stefan Andersson-Engels and Dr. Haichun Liu, for letting me be member of their esteemed research group. I cannot thank you enough for your encouragement that made me feel confident throughout this thesis work. Your patience and continuous support meant a lot to me.

Dr. Diana Thomas and Dr. Sylvio Haas to whom I am deeply grateful not only for your precious help regarding XRD measurements of nanoparticles but also for your sincere friendship that was glorified by delicious pizzas, sweet cookies alongside a cup of strong coffee. This thesis wouldn't mean anything without your assistance.

I would also like to thank everyone from Genovis AB, for letting me use their laboratories and instruments for the production of nanoparticles. Working in such a friendly environment full of extremely helpful professionals who share their experiences with no hesitation has been a privilege for me.

Johan Thorén, my classmate, who never deprived me of his amazing coding skills for all kind of MATLAB problems is very much appreciated.

Additionally, members of Biophotonics group, I want to thank all of you, for your friendship, and also for serious and at the same time funny discussions that we had at Wednesday meetings.

Special thanks to all dear people in Radio Paradise, you cannot imagine how many nights you managed to keep me awake in front of a computer screen by means of your gorgeous playlists.

Furthermore, I want to proclaim my special thanks to my teammates and my coaches from FC Helsingkrona. Your amazing talent that is capable of taking out a joyful part from even the most stressful moments will always be remembered.

Finally, I would like to express my deepest gratitudes to my lovely family for their unconditional love and support.

Abbreviations

Ar	argon
CW	continuous wave
ESA	excited state absorption
ETU	energy transfer up conversion
GS	ground state
GSA	ground state absorption
IR	infrared
Ln	lanthanide
NH_4F	ammonium fluoride
NaCl	sodium chloride
NaOH	sodium hydroxide
NC	nanocrystal
NIR	near infrared
OA	oleic acid
ODE	octadecene
PDT	photodynamic therapy
RE	rare earth
QD	quantum dot
QY	quantum yield
TEM	transmission electron microscopy
Tm^{3+}	trivalent thulium ion
$TmCl_3$	thulium(III) chloride
UC	upconversion
UCNP	upconverting nanoparticle
XRD	x-ray diffraction
YCl_3	yttrium(III) chloride
Yb^{3+}	trivalent ytterbium ion
$YbCl_3$	ytterbium(III) chloride

Contents

Chapter 1

Introduction

There have been many applications that exploit the advantages of upconverted radiation since the discovery of the UC mechanism in 1966. Upconverted radiation is a consequence of a process where less energetic radiation is converted to more energetic radiation. Thus far, remarkable spectroscopic outcomes of radiation conversion pioneered the development of miscellaneous optical devices, such as infrared (IR) quantum detectors, temperature sensors, solid-state lasers, solar cells. Since the synthesis of first nanoparticles that show UC radiation capability, utilization of UCNPs has started to become a hot topic in many different fields of medicine and biology, i.e., biosensing [1], bioimaging [2, 3], and photodynamic therapy (PDT) [4, 5]. Particularly in bioimaging, UCNPs, due to their attractive properties, are regarded as promising contrast agents and luminescent biomarkers compared to conventional quantum dots (QD) and organic fluorophores. UCNPs can be excited by near infrared (NIR) radiation. Since NIR radiation is within the limits of the tissue optical window, Stokes-shifted autofluorescence generated by the biomolecules in the tissue is weak. Due to low background light from luminescent biological tissue components, the signal to background ratio is enhanced yielding high sensitivity imaging of UCNPs. Additionally, as a direct consequence of NIR, high light penetration depth is achieved. Furthermore, a low power density ($\sim$1 Wcm^{-2}) NIR CW laser is sufficient to initiate UC processes of the nanoparticles in which no photo damages to tissues are expected in biological applications. Additionally, UCNPs are able to generate multi-color UC emission bands simultaneously making multi-labelling feasible inside a tissue.

Despite many promising characteristics of UCNPs, there are still challenging constraints that have to be surmounted wisely. First of all, small sized particles, less than 50 nm, are essential for intercellular applications. However, the production of small sized particles with considerably high UC luminescence intensity is a formidable task. Due to the trade-off between the size and UC luminescence intensity, every reduction

in the size of UCNPs yields weaker luminescence intensity. Moreover, the resulting UCNPs may have a hydrophobic nature due to the surfactant material used during the synthesis. Due to indispersibility in water, the biocompatibility of UCNPs is problematic. Furthermore, crystal properties of UCNPs, i.e., morphology, size and phase are significantly associated with the optical properties of the nanocrystal such as UC luminescence intensity, QY, and emission profile. Thus, a rational synthesis method which allows control over morphology, size and phase is required. Herein, an "ideal" UCNP is expected to have the following characteristics: monodispersed, uniform in shape and size, highly crystalline, phase pure, dispersible in water, and strong UC luminescence with multi-emission bands. Thus far, among many other synthesized UCNPs, β-$NaYF_4$ is mainly used as host material providing high QY and UC efficiency [6],[7]. In addition, different chemical methods including thermal decomposition, hydro(solvo) thermal, and coprecipitation have been utilized for the synthesis of UCNPs.

In this thesis work, a modified solvothermal synthesis method is utilized for the synthesis of core $NaYF_4$:Yb^{3+}, Tm^{3+} UCNPs and core-shell $NaYF_4$:Yb^{3+}, Tm^{4+}@ $NaYF_4$ UCNPs and will be outlined in **Chapter 4**. Additionally, analysis results regarding shape, size and phase of the resulting UCNPs will be presented in **Chapter 5**. Furthermore, thermal stability of the crystal phase in UCNPs is examined and the obtained results during a post heating treatment where temperature is increased up to 700°C will be evaluated in **Chapter 5**. As a last study of this thesis work, the feasibility of an enhancement on QY in core $NaYF_4$:Yb^{3+},Tm^{3+} UCNPs is investigated by utilizing a pulse excitation source and the results are presented in **Chapter 5**.

Chapter 2

Upconversion Mechanism

UC is a nonlinear optical process. Higher energy photon emission is achieved as a consequence of a stepwise excitation of light by a single ion *via* either the successive absorption of more than one lower energy photon or the energy transfers between ions. In 1966, the formulation of UC mechanism was submitted separately by Ovsyankin and Feofilov, and Auzel almost seven years after the inspired publication of Bloembergen [8],[9],[10],[11].

2.1 Upconversion processes

UC of radiation is achieved by different processes including excited state absorption (ESA), cooperative upconversion and energy transfer upconversion (ETU). The distinctive characteristics of each UC process will be reviewed in the following subsections by means of the formulations of Auzel [12].

2.1.1 Excited state absorption

A simplified three-level energy system is illustrated in **Figure** 2.1 to facilitate the understanding of an ESA process.

First, the ion jumps up to one of its low-lying long-lived excited state (E1) *via* ground state absorption (GSA). The long-lived nature of this intermediate state reduces the spontaneous emission decay rate of E1 and provides ample time to accommodate at that state. Meanwhile, a second photon reaches and promotes that ion in E1 to the high-lying excited state (E2). Next, the UC luminescence is generated as the ion decays from E2 to ground state (GS).

It is worth mentioning that not only the energy difference between GS and E1 but also between E2 and E1 is required to be nearly equal for an efficient stepwise excitation. This is a significant criterion that should be taken into account for a dopant ion selection that is mainly responsible for UC luminescence.

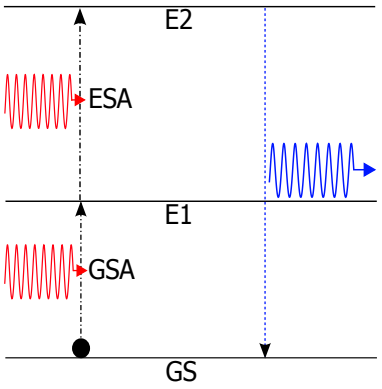

FIGURE 2.1: *Schematic representation of a ESA process in a three-energy level system.*

2.1.2 Energy transfer upconversion

Similar to ESA, there is a sequential excitation of an ion in ETU. In **Figure** 2.2, the ETU process is demonstrated. Here two different types of ion are present. The ion that is responsible for the absorption of the excitation photons, acting as the donor ion in the subsequent non-radiative energy transfer, is called the sensitizer. The neighbouring ion that accepts the transferred energy, undergoes a stepwise excitation resulting in UC luminescence. This is called the activator.

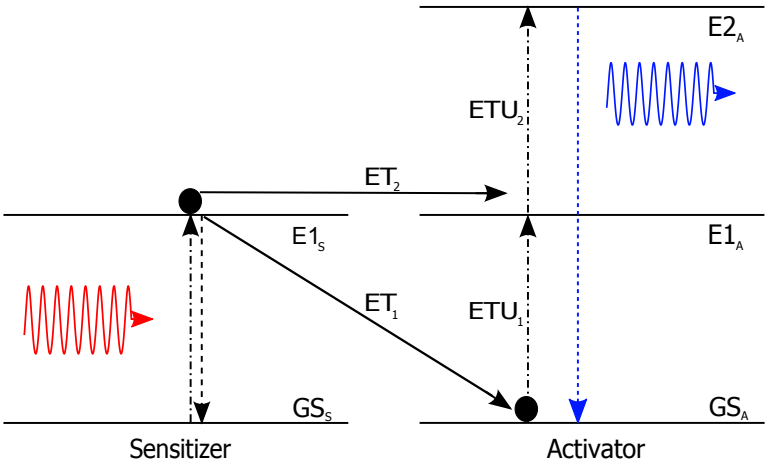

FIGURE 2.2: *The schematic representation of ETU mechanism. Energy transfer (ET) is non-radiative and there is no intermediate photon generation. Herein, ET also occurs in a resonant way by means of equidistant energy level separation.*

There are various types of energy transfer between two neighbouring ions, as demonstrated in **Figure** 2.3. In resonant radiative energy transfer, energy is transferred to the activator by the assistance of a photon originating from the spontaneous decay of the excited sensitizer. The probability of the radiative energy transfer between two neighbouring ions is expressed as follows [13]

$$\rho_{SA}(R) = \frac{\sigma_A}{4\pi R^2 \tau_S} \int \rho_S(\nu)\rho_A(\nu)\, dx, \tag{2.1}$$

where R represents the distance between two neighbouring ions, τ_S defines lifetime of the excited state of the sensitizer, ρ_A is the absorption cross section of activator, ρ_B is the absorption cross section of sensitizer and the integral term defines the spectral overlap between the absorption spectrum of the activator and the emission spectrum of the sensitizer.

In a resonant non-radiative energy transfer, no photon is involved for the energy transfer from one ion to another. The possibility of a non-radiative energy transfer between two neighbouring ions is written as [14]

$$\rho_{SA} = \frac{(R_0/R)^S}{\tau_S}, \tag{2.2}$$

where R_0 is the critical distance between two neighbouring ions and S is the parameter that takes an integer number depending on the type of the electronic interaction between the transition dipoles of the neighbouring ions.

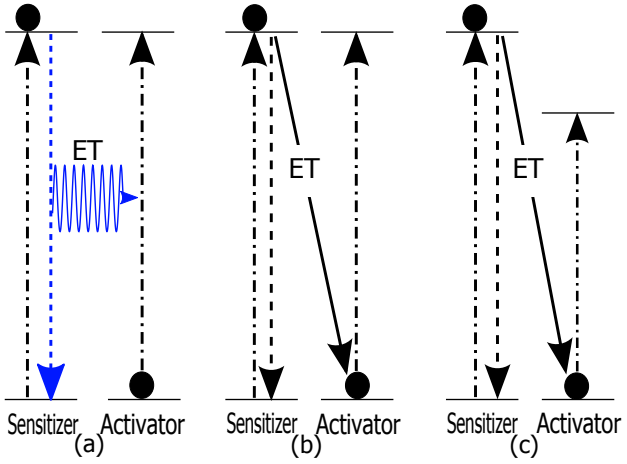

FIGURE 2.3: *A scheme that includes different energy transfer pathways between the neighbouring ions: (a) Resonant radiative transfer. (b) Resonant non-radiative transfer. (c) Non-radiative transfer by phonon assistance.*

Unlike the resonant energy transfers in **Figure** 2.3 (a) and (b), transfer of the energy may have non-resonance characteristic. Non-resonant energy transfer may occur between the neighbouring ions that have dissimilar energy level structure. In **Figure** 2.3 (c), it is clearly seen that there is energy mismatch between the excited states of the activator and the sensitizer. In such a case, phonons assist to overcome the mismatch energy in which energy transfer is subsequently completed. The number of phonons that involve in the energy transfer depends on the magnitude of the energy mismatch [15].

2.1.3 Cooperative upconversion

Cooperative upconversion comprises the two different energy transfer processes that are known as cooperative sensitization and cooperative luminescence. In **Figure** 2.4 the

schematic representations of these processes are shown.

In cooperative sensitization, required energy for the excitation of the activator is provided by simultaneous energy transfers from two or more sensitizers. Thereby, the activator generates UC luminescence as a result of the temporal overlap of energy transfer. However, in the case of cooperative luminescence, two excited ions combine their energy and emit one photon. Thus, it is not regarded as a transfer, rather is an accumulation of energy at a time.

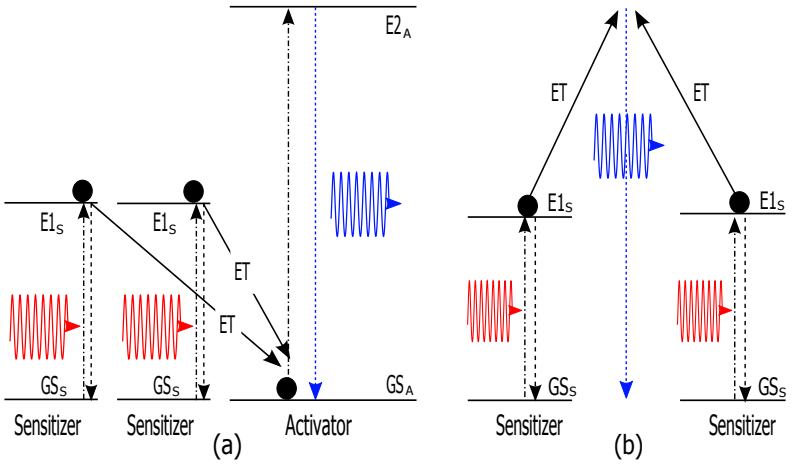

FIGURE 2.4: *The schematic representation of (a) cooperative sensitization, (b) cooperative luminescence.*

To sum up, ETU has the highest UC efficiency among all UC processes described above. The UC efficiency in ETU is two orders of magnitude higher than ESA and 4-5 orders of magnitude higher than cooperative UC processes [12]. ETU efficiency is even much higher than common nonlinear optical processes such as second harmonic generation and two-photon absorption [12].

2.2 Excitation Power Dependence of Upconversion Luminescence Intensity

The UC luminescence intensity is dependent on the excitation power density. The excitation power dependence of UC luminescence intensity can be understood by means of a model first presented by Pallnau *et al* [16]. The model is illustrated in **Figure** 2.5. The analysis of power dependence is based on a set of rate equations at high and low excitation power regimes. Rate equations describe here the optical processes for energy states of the activator including UC process, spontaneous emission and multi-phonon relaxation. By means of rate equations, the steady state population density of an energy state can be found. Since the population density of an energy state is associated with luminescence intensity, the excitation power dependence of UC luminescence is subsequently revealed.

Prior to the rate equation analysis is introduced, I would like to outline the assumptions made in this model:

- Cross-relaxations do not occur.
- No emission occurs due to the transitions from a high-lying excited to a low-lying excited state, e.g. $E2_A$-$E1_A$ transition.
- The ground state population is not varying; negligible bleaching.
- Successive excitation of the activator is carried by solely ETU processes.
- The energy separations between the adjacent energy states of the activator are equal. Additionally, the same energy separation holds for the gap between the excited state and ground state of the sensitizer.
- Only the sensitizer absorbs the excitation photons.

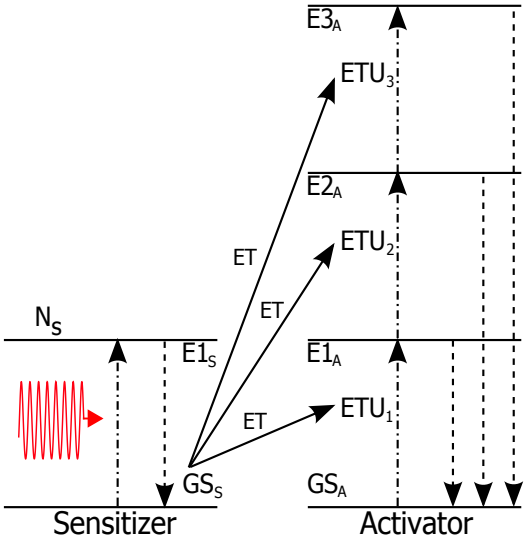

FIGURE 2.5: *The scheme of the model based on sensitizer-activator configuration is shown. The energy transfer is carried out sequentially. Thus, successive ETU processes take place in the activator.*

The steady-state population density of the excited state of the sensitizer (N_S) is given by

$$N_S = \rho P, \tag{2.3}$$

where P, and ρ denote the exitation power and the excitation cross-section of the sensitizer ions, respectively. **Equation** 2.3 is the direct consequence of the assumption of a constant ground state population density. Let's assume an activator with i energy states. The steady state population densities of these states are denoted by N_i. Moreover, the ETU rate from energy state i to energy state $i+1$ of the activator is expressed by W_i. In addition, R_i denotes the relaxation rate constant from energy state i to the ground state of the activator (GS_A). By means of these definitions, the following relation may be written:

$$N_1 \propto N_S \propto P \tag{2.4}$$

The rate equation for the steady state population density of energy state i of the activator is written down as

$$W_i N_i N_S + R_i N_i = W_{i-1} N_{i-1} N_S \tag{2.5}$$

Equation 2.5 yields the population density of energy state i in steady state as

$$N_i = \frac{W_{i-1} N_{i-1} N_S}{R_i + W_i N_S} \tag{2.6}$$

Herein, the rate equation analysis will be examined in two regimes of the excitation power: Low excitation power, high excitation power.

2.2.1 Low power regime

As the excitation power is low, the depletion of i^{th} energy state is dominated by the relaxation process instead of the ETU. Since $R_i \gg W_i N_S$, the ETU term in **Equation** 2.5 becomes negligible. Thereby, **Equations** 2.5 and 2.6 become respectively:

$$W_{i-1} N_{i-1} N_S = R_i N_i, \tag{2.7}$$

$$N_i = \frac{W_{i-1} N_{i-1} N_S}{R_i}. \tag{2.8}$$

There is a linear dependence between the population density of the state i and the population density of the state i-1 multiplied by N_S. The same relation holds for the population density of the state i-1 and the population density of the state i-2 multiplied by N_S. Since the same relation could be applied to all excited states, the result can be written as follows

$$N_i \propto (N_S)^i \propto P^i \tag{2.9}$$

Equation 2.9 implies that if one plots a graph of the UC luminescence intensity in a double-logarithmic representation versus the excitation power, the slope of that graph would be i. It additionally gives the number of ETU processes needed for a certain UC luminescence profile. The relation in 2.9 is also interpreted as an outcome of a measurement for the number of photons involved for the stepwise excitation of the activator in UC process (In this case, it is ETU).

2.2.2 High power regime

As the excitation power is sufficiently high, the ETU becomes dominant over the relaxation process. This means $W_i N_S \gg R_i$. Hence, **Equations** 2.5 and 2.6 are written respectively as follow

$$W_{i-1} N_{i-1} N_S = W_i N_i N_S \tag{2.10}$$

$$N_i = \frac{W_{i-1}}{W_i} N_{i-1} \tag{2.11}$$

and when $N_i \propto N_{i-1}$ is combined with **Equation** 2.4, the result is written as

$$N_i \propto (N_S)^i \propto P^1 \tag{2.12}$$

In **Equation** 2.12, it is clearly seen that population densities of all energy states of the activator have the same power dependence in the high power regime. The slope of the UC luminescence intensity versus the excitation power graph will be equal to one regardless of the number of ETU processes. It states that the nature of power dependence on UC luminescence intensity is linear as excitation power density is high. It is worth mentioning that similar rate equation analyses have been utilized in **Paper I** to figure out suitable pulse laser parameters to be able to enhance QY in core NaYF4:Yb^{3+},Tm^{3+} UCNPs.

In general, sensitizer and activator have dissimilar energy level structure, in which the model explained above would be no longer used. For such a case, another rate equation model is presented [17].

2.3 Quantum Yield of Upconverting Nanoparticles

The ratio between the number of emitted photons (N_{em}) and the number of absorbed photons (N_{abs}) is known as the internal QY (η). This is mostly defined in percent. The parameter is characterized as

$$\eta = \frac{N_{em}}{N_{abs}} = \frac{k_0 I_{em}}{I_{ex}} \tag{2.13}$$

where k_0 is a scaling factor, I_{em} ($\mathrm{Wcm^{-2}}$) is the intensity of emission and I_{ex}($\mathrm{Wcm^{-2}}$) is the intensity of excitation.

As shown in the previous section, the intensity dependence of a two-photon UC emission based on the ETU has a quadratic nature at low excitation power densities, whereas it turns into a linear form at high excitation power densities. The saturation characteristic of UC luminescence with increasing excitation power density has been used to figure out QY of NIR UC emission of core $NaYF_4$:Yb^{3+},Tm^{3+} UCNPs as part of this thesis work and the results are presented in **Paper I**.

2.4 Building Blocks of Upconverting Nanoparticles

There are two main building blocks of a typical upconverting luminescent particle: Inorganic host crystal and dopant ions. Some inorganic host crystals, e.g. $NaYF_4$ crystal, may not display UC luminescence by itself in which may require doping to be luminescent. Thus, by the presence of a dopant ion, e.g. Tm^{3+} in $NaYF_4$:Tm^{3+}, the entire crystal may become luminescent. Although one type of dopant ion is generally sufficient to generate UC luminescence, two different types of ions are favourable for higher UC

luminescence. As previously mentioned ETU is the most efficient UC process where two different types of dopant ions as being sensitizer and activator are required.

Recall that Yb^{3+}(sensitizer)/Tm^{3+}(activator) co-doped $NaYF_4$ is UCNP that has been under the study at this thesis work. Trivalent Yb-Tm pair is selected due to their promising features as dopant ions which will be outlined in the following subsections.

2.4.1 Activator

The distinctive role of an activator in the UC process has been explained previously. Simply, the activator is the ion that undergoes a series of sequential excitation and then reaches a high-lying excited state where UC luminescence is generated. An activator ion has to possess an energy level structure with multiple long-lived excited states. Equidistant energy separations between excited states of the activator ion are favourable in which ETU may take place efficiently.

Some of the elements in the lanthanide group are regarded as good activators due to their exceptional energy level structure. $[Xe]4f^n6s^2$ represents electronic configuration of most of lanthanide atoms including holmium (^{67}Ho), erbium (^{68}Er), and thulium (^{69}Tm). In addition, all lanthanide atoms have very stable +3 oxidation state in which they may exist as trivalent ions [18]. As for emission profile, sharp and narrow emission bands corresponding to NIR and the visible region are obtained due to f-f transitions in lanthanides. The fact that f-f transitions have low probability to occur due to the Laporte rule turns out to be an advantage for UC. Low probability of f-f transitions imply that energy states have long lifetimes which favour UC.

Therefore, Tm^{3+}, Er^{3+} and Ho^{3+} are among the most suitable activator ions owing to their ladder-like energy level structure that enables an efficient ETU process.

As known, the multi-phonon relaxation is an undesired process which depopulates the excited state, thereby weakens the UC luminescence. The multi-phonon relaxation rate for 4f levels of RE ions can be described by an exponential relation with the energy gap [19]

$$k_{NR} = \beta e^{-\alpha \Delta E}, \tag{2.14}$$

where α and β are constants. **Equation** 2.14 implies that the multi-phonon relaxation rate decreases exponentially with increasing energy separation between an excited state and either another low-lying excited state or ground state. Due to low ΔE values of Ho^{3+} ion, trivalent Er and Tm ions are among the most utilized ions as an activator in UCNPs.

2.4.2 Sensitizer

As mentioned previously, UC of radiation could be realized by exploiting even one type of dopant ion. In a singly doped nanocrystal, dopant ions are responsible for all optical

processes including the absorption of pump photons, UC processes, and luminescence. Thus, the dopant ion is expected to function as both sensitizer and activator at a time. Nevertheless, promising activator ions, e.g. Tm^{3+} and Er^{3+}, are infertile as being sensitizers due to their low absorption cross-section, particularly in NIR range.

Low pump photon absorption disfavours weak UC luminescence in which high photon absorption is a significant criterion to be fulfilled by a dopant ion. In a singly doped nanocrystal, the low photon absorption problem would be surpassed by increasing the concentration of the dopant ion [18]. However, when the number of the dopant ions is increased, they get closer to each other which facilitates the non-radiative energy losses such as the cross-relaxation.

Therefore, instead of a direct excitation of the activator ions *via* the pump photons, the sensitizer with relatively high absorption cross-section is utilized to excite the activator ion *via* energy transfer. Furthermore, in the presence of a sensitizer ion along the activator ion, the most efficient UC process, ETU, becomes feasible.

Trivalent ytterbium (Yb^{3+}) ion is one of the most common sensitizer owing to its distinctive energy level structure and relatively high absorption cross-section in NIR region. As for energy level structure of Tm^{3+}, there is only one excitable 4f state ($^2F_{5/2}$), to which a transition from ground state ($^2F_{7/2}$) is accomplished by the absorption of NIR photons. In addition, the energy structure of Yb^{3+} is well suited to the energy structure of the prevalent activators, e.g. Tm^{3+} or Er^{3+}.

Different trivalent lanthanide ions are capable of displaying specific emission bands ranging from the NIR to UV due to their unique energy level arrangement. Therefore, sensitizer-activator ion pair should be wisely selected with regard to the type of the application where they are utilized.

2.4.3 Host crystal

As for UCNPs, the selection of a suitable host material has always been an important issue. Basically, two characteristics are required from a crystal material to be said "*ideal*" host crystal. Firstly, the lattice size of the host crystal should be in a close match with that of dopant ions. Secondly, low phonon energy of a host crystal is favourable. Low phonon energy nature decreases non-radiative losses during UC processes, which enables a radiative emission rate. Many different materials are utilized as host crystal including heavy halide based crystals, oxide based crystals, and fluoride based crystals [18, 20, 21]. On the other hand, hygroscopic nature of those heavy halides makes them impractical although they have low phonon energies less than 300 cm^{-1}. Furthermore, oxide based crystals with high chemical stability mostly suffer from their high phonon energy that is generally larger than 500 cm^{-1}. Nonetheless, the fluoride based crystal material

$NaYF_4$ with hexagonal crystal structure is yet considered as one of the most efficient host material owing to its chemical stability and its relatively low phonon energy [22].

Chapter 3

Synthesis Methods

Various chemical methods including coprecipitation, thermal decomposition [23], hydro(solvo) thermal method [24], sol-gel processing [25], combustion synthesis [26] and flame synthesis [27] have been developed over the years in order to synthesize more efficient and high quality UCNPs. Among these methods, coprecipitation, thermal decomposition and hydro(solvo)thermal methods find wider use due to their remarkable advantages. In this thesis work, all UCNPs were synthesized by the solvothermal method. The steps of this method will be outlined in details in **Chapter** 4.

In each synthesis method, experimental parameters, e.g. reaction time and temperature, may affect the crystal properties of UCNPs such as size, phase and shape. Moreover, different solvents, surfactants, and the fluorine sources are used during the synthesis method to vary the crystal properties. Optical properties of UCNPs are affected by the changes in the crystal structure properties [2, 6]. Thus, it is essential to have a precise control over the synthesis method in which the experimental parameters are required to be set wisely for high quality nanoparticles.

3.1 Thermal Decomposition Method

Thermal decomposition of organic precursor(s) such as metal trifluoroacetate(s) (TFA) is one of the well-known approaches for the controlled synthesis of uniform, well-shaped and high quality crystalline nanoparticles.

The basic idea behind this approach is based on the decomposition reaction of metal TFAs in a non-coordinating solvent, e.g. octadecene (ODE), with the assistance of a surfactant, e.g. oleic acid (OA), at certain elevated temperatures mostly between 250°C and 330°C. This approach was firstly applied to the synthesis of single crystalline monodispersed LaF_3 triangular nanoplates with solely the presence of one type of organic precursor by Zhang *et al* [28]. Subsequently, a slightly modified method was proposed, where different types of rare earth metal TFAs decomposed and yield cubic phase (α)

$NaYF_4$ nanoparticles co-doped with either Er^{3+}-Yb^{3+} ion pair or Tm^{3+}-Yb^{3+} ion pair [29].

Due to the pyrolysis of air sensitive-metal TFAs, various fluorinated and oxyfluorinated carbon species come out as intermediate products; these are known to be extremely toxic. Thus, the thermal decomposition method suffers from toxic by-products. Even though high quality, monodispersed nanoparticles are promised by this method, the resulting nanoparticles still have cubic phase structure. Ln doped β-$NaYF_4$ UCNPs have higher UC luminescence intensity compared to Ln doped α-$NaYF_4$ UCNPs [30]. Therefore, Ln doped $NaYF_4$ UCNPs with cubic crystal phase are not favourable. Additionally, the thermal decomposition method has a disadvantage of requiring surface modification of the resulting nanoparticles. The usage of OA as a surfactant yields hydrophobic nanoparticles in which the surface modification for the nanoparticles is essential to make them hydrophilic, and so biocompatible.

3.2 Hydro(Solvo)thermal Method

The hydro(solvo)thermal method has been frequently used to produce both α-phase and β-phase lanthanide doped $NaYF_4$ nanoparticles. As opposed to the thermal decomposition method, the synthesis of nanoparticles with controlled crystal size, shape and good dispersibility is performed at low reaction temperatures, e.g. below 230°C.

The hydrothermal method is based on a set of chemical reactions where a mixture of rare earth precursors with a surfactant that reacts with certain metal and fluorine ions in an aqueous solution. Nevertheless, specialized reaction vessels, namely autoclaves, are required to carry out all these chemical reactions under a certain pressure and temperature that are above a critical point of the solvent over a long period of time. In many cases, water is utilized solely as a solvent but strong solvents including acetic acid and ethanol may replace the water in order to increase the reaction speed, and so the solubility. In the cases where a strong solvent is present, the method is generally renamed as solvothermal instead of hydrothermal.

β- $NaYF_4$:Yb^{3+},Er^{3+} UCNPs with good dispersibility and high UC luminescence were successfully synthesized in either hydrothermal conditions or solvothermal conditions [31]. The crystal size is controlled by varying the molar ratio between surfactant and Ln^{3+} ion. In the solvothermal method, a shape modulator, e.g. CTAB, can diversify the shape of nanoparticles including rod, worm-like and spherical. On the other hand, it has a negligible effect on the shape of nanoparticles at hydrothermal conditions. In addition, a shape modulator is exploited alongside a strong solvent, e.g. ethanol, to gain more control over the shape of the nanoparticles [31].

Since highly crystalline, uniform in size β- $NaYF_4$:Yb^{3+},Er^{3+} nanoparticles are produced either hydrothermally or solvothermally, no post-heating treatment for a phase

transformation is required. On the other hand, the hydro(solvo)thermal method suffers from drawbacks including autoclave necessity and long lasting chemical reactions which may last for days.

3.3 Coprecipitation

Coprecipitation is one of the most common methods to synthesize crystals of uniform small-sized Ln^{3+} doped UCNPs are synthesized. There is no need of complex chemical procedures and costly experimental tools [18].

In general, shape and size of UCNPs are controlled by the assistance of ligands and surfactants but the simultaneous control of both phase and size or shape is not feasible. Thus, the coprecipitation method is required to be coupled with post-annealing process.

A size controlled synthesis of α-$NaYF_4$:Yb^{3+},Er^{3+} nanoparticles regardless of shape was performed *via* coprecipitation [32]. As an efficient chelator for rare earth ions is used, a stable metal-surfactant complex is formed. Thus, for UCNPs a distinct separation of nucleation and growth stages are provided, which is known as the very first requirement of crystal uniformity postulated by the LaMer Model [33]. Although the surfactant may play a size modulator role resulting in smaller sized UCNPs, weak UC luminescence intensity is still a problem due to α-phase nature of UCNPs. Therefore, a post-heating treatment at high temperature levels, e.g. between 400°C-600°C, is necessary in order to initiate a phase transition from cubic to hexagonal. As a result of that, the UC luminescence intensity gets ∼40 fold stronger [32]. However, at the end of the post-heating treatment, an increase in size of UCNPs is obtained, which makes them mostly impractical for intracellular applications. It is clearly seen that there is a trade-off between small size and hexagonal phase formation, and so between the biocompatibility and strong UC luminescence intensity.

Chapter 4

Synthesis Protocol

In this chapter, the synthesis protocol based on the solvothermal method will be outlined in details. The synthesis of 1 mmol core $NaYF_4$:Yb^{3+},Tm^{3+} UCNPs were performed as the molar ratio of the reagents set to YCl_3:$YbCl_3$:$TmCl_3$=74.7:25:0.3. In this synthesis method, NaOH, OA-ODE and NH_4F were used as sodium ion source, surfactant-solvent pair and fluoride source, respectively. The core $NaYF_4$:Yb^{3+},Tm^{3+} UCNPs were synthesized by the following protocol that is a slightly modified version of the protocol proposed by Li *et al* [34].

4.1 Synthesis of Core $NaYF_4$:Yb^{3+},Tm^{3+} Upconverting Nanoparticles

At room temperature, 0.747 mmol (146.4 mg) YCl_3, 0.25 mmol (69.5 mg) $YbCl_3$ and 0.003 mmol (0.83 mg) $TmCl_3$ were added to a 50 mL round bottom three-necked flask with 6 ml OA and 17 ml ODE. The entire mixture inside the flask was heated up to 145.5°C during 60 minutes under vigorous stirring to form a homogeneous light yellow mixture. As the mixture was being heated, vacuum condition was provided *via* a vacuum pump. The mixture was maintained at 145.5°C for another 60 minutes under vacuum condition to make sure that all reagents were completely dissolved in the solvent. It is worth mentioning here that vigorous stirring was being maintained throughout the entire synthesis unless otherwise stated. At the end of 60 minutes, the initial turbid mixture became transparent and light yellow in colour. Subsequently, the entire mixture was allowed to cool down naturally to room temperature under atmospheric pressure after the disconnection of the vacuum pump.

Meanwhile, a mixture of 2.5 mmol (100 mg) NaOH and 4 mmol (149.1 mg) NH_4F in 10 ml methanol was prepared at room temperature and subsequently 60 minutes ultrasonication was carried out for complete dispersion of NaOH and NH_4F in methanol.

The mixture of NaOH and NH_4F in 10 ml methanol was added to the solution of RE chlorides ($RECl_3$, in our case RE=Y,Yb,Tm) in OA-ODE mixture inside the flask at room temperature to form inorganic $NaYF_4$ crystal nuclei. This mixture was maintained at room temperature for 30 minutes. Subsequently, the mixture was heated up to 110°C by a rate shown in **Table** 4.1 in order to evaporate all methanol. A constant temperature increase in a constant time interval favours the formation of high crystalline UCNPs. A fast methanol evaporation is not favourable in this step. It affects the crystal growth of UCNPs resulting in no nanocrystal formation. If methanol is not removed completely in this step, the turbid solution will not become translucent. The unsuccessful removal of methanol hinder the nucleation stage of UCNPs resulting in no crystal formation. The complete evaporation of methanol was achieved as seen as the turbid solution turned out to be completely translucent.

Temperature Interval [$°C$]	Time Elapsed [mins]
30$\Longrightarrow$40	16
40$\Longrightarrow$50	14
50$\Longrightarrow$60	8
60$\Longrightarrow$70	7
70$\Longrightarrow$80	12
80$\Longrightarrow$90	18
90$\Longrightarrow$100	13
100$\Longrightarrow$110	10
Total Reaction Time	98

TABLE 4.1: *Methanol evaporation rate*

For the solution, the temperature was stabilized at 110°C for another 30 minutes under argon (Ar) gas atmosphere. A condenser was connected to the flask for cooling in the next step. Subsequently, the solution was heated up to 298°C where nanocrystal growth of $NaYF_4$:Yb^{3+},Tm^{3+} began. The reaction was maintained at 298°C for an optimized reaction time of 65 minutes. Finally, the solution was allowed to cool down to room temperature.

For high quality UCNPs, a precise control of temperature is required for both the crystal nucleation stage and crystal growth stage. Throughout the synthesis, temperature fluctuations were controlled to remain within ±2°C. More temperature fluctuations affect both the crystal phase and the size of UCNPs.

In order to remove possible undesired impurities e.g. sodium chloride (NaCl) crystals and OA residues inside the resulting mixture, a "washing" procedure was carried out at room temperature. The resulting mixture was mixed with 21 ml ethanol. After a few minutes under vigorous stirring, it was placed into the centrifuge for 10 minutes to complete the precipitation of UCNPs. Subsequently, the supernatant was discarded yielding solely the presence of UCNPs at the bottom of the test tube. Remaining UCNPs

were mixed with 40 ml ethanol yet again and were precipitated *via* centrifugation in 10 minutes. Again, the supernatant was removed from the resulting solution and 1 ml hexane as a non-polar solvent was added to the test tube where only UCNPs were present.

Eventually, the dispersion of $NaYF_4$:Yb^{3+},Tm^{3+} UCNPs began as a consequence of hexane addition, thereby forming homogeneous light yellow colloidal solution.

4.2 Synthesis of Core-Shell $NaYF_4$:Yb^{3+},Tm^{3+}@$NaYF_4$ Upconverting Nanoparticles

Core-shell $NaYF_4$:Yb^{3+},Tm^{3+}@ $NaYF_4$ UCNPs having different shell thickness were synthesized by a seeded growth approach where undoped $NaYF_4$ crystals grow on the surface of the seed crystals, $NaYF_4$:Yb^{3+},Tm^{3+} at high temperature. Undoped $NaYF_4$ shell thickness was controlled by changing the concentration of the YCl_3 reagent whilst keeping the molar ratio of reagent (YCl_3), fluoride source (NH_4F) and sodium ion sources (NaOH) as 1:4:2.5. The same molar ratio had been used in the synthesis of core UCNPs by Qian and Zhang, and Wang *et al* [30, 35]. In addition, the YCl_3 concentration was adjusted to be 0.20 mmol, 0.40 mmol, 0.60 mmol and 0.80 mmol in order to form four core-shell UCNP samples that are sample A, B, C, and D with each different shell thickness. Herein, only the synthesis of core-shell $NaYF_4$:Yb^{3+},Tm^{3+}@$NaYF_4$ UCNPs of sample A with 0.20 mmol YCl_3 consumption is explained. Even though the same protocol holds for the synthesis of three other samples of core-shell UCNPs, a few steps of the synthesis protocol was adjusted for samples B, C, D. Firstly, the methanol evaporation rate was different in each synthesis. Secondly, the evaporation rate on the nucleation phase was not constant for every core-shell UCNPs.

At room temperature 0.20 mmol (39.30 mg) YCl_3 was added to 50 ml round bottom three-necked flask with 6 ml OA and 17ml ODE at room temperature. The vacuum pump was connected to the system, the entire mixture was heated up to 150°C during 60 minutes under vigorous stirring. For another 60 minutes the mixture was maintained at 150°C for the formation of the clear light yellow solution to be observed. Subsequently, the mixture was left for cooling naturally after the vacuum pump was removed from the system. Previously synthesized core $NaYF_4$:Yb^{3+},Tm^{3+} UCNPs dispersed in 0.2 ml hexane was added to the mixture at room temperature. The mixture temperature was increased to 115°C at a rate shown in **Table** 4.2. The mixture was maintained at 115°C for 30 minutes. Next, the mixture was yet again left for natural cooling to room temperature level under atmospheric pressure.

Meanwhile, 0.80 mmol (29.9 mg) NH_4F and 0.5 mmol (20.3 mg) NaOH mixture was dissolved in 3 ml methanol *via* 60 minutes sonication at room temperature. This

Temperature Interval [°C]	Time Elapsed [mins]
50⟹60	10
60⟹70	9
70⟹80	12
80⟹90	11
90⟹100	12
100⟹115	10
Total Reaction Time	64

TABLE 4.2: *Heat rate at the beginning of the crystal nucleation stage*

reactant mixture was subsequently added to the flask and was maintained at room temperature for 30 minutes. After Ar gas flow was given to the system, the mixture was heated up to 115°C at a rate shown in **Table** 4.3. The mixture was maintained at 115°C for 45 minutes.

Temperature Interval [°C]	Time Elapsed [mins]
50⟹60	8
60⟹70	8
70⟹80	7
80⟹90	7
90⟹100	9
100⟹115	11
Total Reaction Time	50

TABLE 4.3: *Methanol evoparation rate for $NaYF_4$:Yb^{3+},Tm^{3+}@$NaYF_4$ NCs.*

For the crystal growth stage, the mixture at 115°C temperature level was further heated up to 298°C, where the reaction time was set to 75 minutes. Subsequently, the resulting mixture was cooled down to room temperature level where the washing procedure was started.

Similar to the washing procedure of core UCNPs, the same amount of ethanol was consumed. Although every single step of washing procedure of core UCNPs was applied to the core-shell washing procedure, the amount of hexane for the dispersion of $NaYF_4$:Yb^{3+},Tm^{3+}@$NaYF_4$ UCNPs was slightly changed from 0.4 ml to 1 ml.

Finally, five different samples were obtained: One sample of core $NaYF_4$:Yb^{3+},Tm^{3+} nanoparticles and four samples of core-shell $NaYF_4$:Yb^{3+},Tm^{3+} @$NaYF_4$ nanoparticles. Note that, the UCNP shell thicknesses are supposed to be different. Similarly, an unavoidable fluctuation in the reaction temperature throughout the synthesis of core-shell UCNPs was kept within a 2°C temperature margin.

Chapter 5

Measurements and Results

Measurements and results regarding the analysis of crystal properties of UCNPs in the samples of core, core-shell A, core-shell B, core-shell C, and core-shell D will be presented in this section. In addition, the XRD patterns of UCNPs in samples A, B, C at elevated temperature levels, which indicate a good thermal stability of the crystal phase of UCNPs will be disclosed. Moreover, simulated QY and experimental UC emission signal gain of the NIR emission in UCNPs will be revealed at the end of this chapter.

5.1 Crystal Structure Analysis of Core and Core-Shell Upconverting Nanoparticles

The analysis of crystal properties covers size, shape, and phase characterization of UCNPs in every sample. The size, shape and phase of core $NaYF_4$:Yb^{3+},Tm^{3+} UCNPs in and core-shell $NaYF_4$:Yb^{3+},Tm^{3+}@$NaYF_4$ UCNPs with different shell thicknesses are characterized by XRD and TEM techniques. XRD measurements at room temperature were performed on a Newport 4-circle diffractometer with kappa geometry, equipped with Titan CCD detector (λ=0.98-1.4 Å) [36]. Additionally, high-resolution TEM images were recorded *via* TEM instrument (JOEL 3000F) to characterize the shape and the size of UCNPs.

For XRD measurements, the core $NaYF_4$:Yb^{3+},Tm^{3+} UCNPs and the core-shell $NaYF_4$:Yb^{3+},Tm^{3+}@$NaYF_4$ UCNPs were dispersed in hexane. Subsequently, the core sample and core-shell samples A, B, C, D were prepared in 0.3 mm quartz-capillaries for size and crystal phase analysis. The X-ray radiation wavelength of the I711 beamline at the MAX II Laboratory was set to 0.992082 Å during XRD measurements of the core and core-shell A,B,C samples. However, the radiation wavelength was shifted to 0.992185 Å for the core-shell sample D.

The data analysis of the resulting XRD patterns was carried out by the softwares, PM2K and MATLAB [37]. The broadening of the diffraction peaks in the XRD patterns

Sample Name	Core Mean Size [nm]	Shell Mean Size [nm]
Core	43.74±2.70	
Core-Shell A	55.44±22.80	1.48±0.21
Core-Shell B	56.69±21.01	9.75±0.12
Core-Shell C	48.27±27.77	12.39±0.24
Core-Shell D	43.00±0.48	17.22±0.04

TABLE 5.1: *Mean size of hexagonal structured core and core-shell UCNPs. Additionally, mean shell thickness of core-shell UCNPs in each sample is explicitly written.*

were analyzed to figure out the size of the corresponding UCNPs. Throughout the size analysis, the crystal shape of the core and the core-shell UCNPs were presumed to be hexagonal. In fact, this could be a good assumption since OA, the surfactant used in the synthesis, is decisive parameter on the shape of UCNPs. Not only the type but also the amount of the surfactant used in the synthesis can change the shape of the particles. Subsequently, it will be seen in TEM images that most of UCNPs are indeed hexagon in shape.

Table 5.1 shows the mean size of UCNPs in the core sample and core-shell UCNPs with different thickness in samples A, B, C and D. The relatively high standard deviations in size of UCNPs in samples A, B and C indicate that the monodispersity of core-shell UCNPs is not as high as expected. This is mainly due to the formation of undesired nanocrystals (NCs) through the core-shell synthesis, shown in **Figures** 5.4 **(a)** and 5.4 **(b)**. These NCs are are identified as non-coated $NaYF_4$ that were expected to be shell around the core but instead became separate NCs. The mean size of these NCs are calculated as $\mathbf{1.72 \pm 0.01}$ nm. However, the core sample has a more uniform size distribution. Since the core NCs in core-shell samples were provided solely from the very same core sample, it implies that the production quality of core NCs is better than that of core-shell NCs. Although the relatively high synthesis quality is achieved on the core NCs, small amount of NCs less than 1 nm in size are observed in the core sample in **Figure** 5.2 **(a)**. These are possibly NaF residues that were not successfully removed during the synthesis washing process.

The crystal phase of the UCNPs at room temperature were characterized by the XRD pattern. The XRD patterns of the core and the core-shell UCNPs are represented in **Figure** 5.1. The position of the diffraction peaks in the corresponding XRD patterns shown in **Figure** 5.1 indicates that UCNPs having hexagonal crystal phase are present. The distinctive diffraction peaks with relatively high intensity at 2θ angle of **19**°, **20**°, **27.5**°, **33.7**° and with relatively low intensity at 2θ angle of **22**°, **29**°, **34.7**°, **38**°, **39**°, **40**°, and **40.4**° are indexed to hexagonal structured UCNPs. In addition, the XRD pattern corresponding to sample B has one different diffraction peak at 2θ angle of **18**° indexed to the NCs having cubic crystal phase with the other common

peaks at 2θ angle of **29**° and **34.7**°. This diffraction peak is the characteristic peak that distinguishes α-$NaYF_4$ NCs from β-UCNPs. Thus, in sample B previously mentioned non-coated $NaYF_4$ NCs with the size of about 1.7 nm are identified to have cubic crystal phase. However, the non-coated $NaYF_4$ NCs in the other samples, i.e., A, C and D are considered to have hexagonal crystal phase due to the overlapping diffraction peak positions in XRD patterns. The formation of the UCNPs having hexagonal crystal phase is significantly important since it is previously stated that β-$NaYF_4$:Yb^{3+},Tm^{3+} UCNPs have higher UC luminescence intensity compared to that of α-$NaYF_4$:Yb^{3+},Tm^{3+} UCNPs. Moreover, the intensity differences in the certain diffraction peaks of each XRD pattern may be seen in **Figure** 5.1. This implies that the number of detected/formed NCs are different in every sample. Since it is not feasible to use the exact same number of core NCs throughout the shell growth of core-shell UCNPs for every sample, intensity differences are expected.

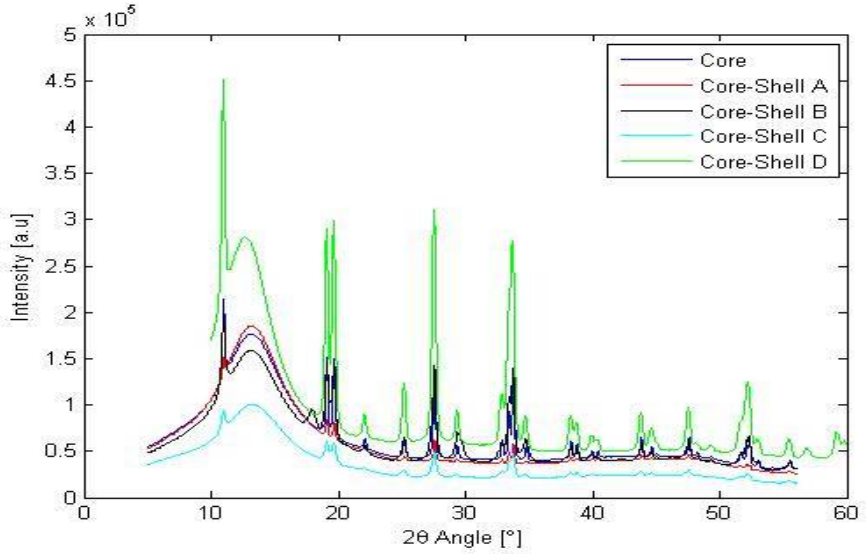

FIGURE 5.1: *The XRD pattern of the non-coated UCNPs in sample core and the shell-coated UCNPs in samples A,B,C,D. The distinctive peak at 2θ angle of 18° implies that there is more than one crystal phase in sample B.*

The lattice parameters of UCNPs in each sample were calculated by the analysis of diffraction peaks in the XRD patterns, and are given in **Table** 5.2 on account of the phase characterization. Unintentionally formed, cubic structured, non-coated $NaYF_4$ NCs in sample B have surely different lattice parameter which is not presented in **Table** 5.2 instead given here as $\boldsymbol{a}$**=0.550013** $\pm$ **0.000011 nm**.

A series of TEM images shown in **Figures** 5.2, 5.3, 5.4, 5.5 and 5.6 is obtained to characterize the shape and the size of UCNPs. According to the presented TEM images, UCNPs in all samples are almost uniform in hexagonal shape. In addition, previously discussed the non-coated undesired NCs with the size of about 1.7 nm are clearly seen in the TEM images. Although the uniformity in shape of UCNPs is as high as expected, a

Sample Name	Core Lattice Parameters [nm]	Shell Lattice Parameters [nm]
Core	a=0.597568 ± 0.000002 c=0.350413 ± 0.000002	
Core-Shell A	a=0.597378 ± 0.000005 c=0.350294 ± 0.000005	a=0.602 ± 0.002 c=0.354 ± 0.002
Core-Shell B	a=0.597803 ± 0.000003 c=0.350550 ± 0.000003	a=0.597898 ± 0.000001 c=0.352685 ± 0.000001
Core-Shell C	a=0.597471 ± 0.000011 c=0.350475 ± 0.000011	a=0.598404 ± 0.000019 c=0.351552 ± 0.000016
Core-Shell D	a=0.597553 ± 0.000011 c=0.350549 ± 0.000009	a=0.600195 ± 0.000015 c=0.351873 ± 0.000011

TABLE 5.2: *The lattice parameters of UCNPs.*

small amount of NCs having spherical shape is present. A closed up figure of a spherical NC is shown in **Figure** 5.3 **(c)**. This could be due to either the unavoidable temperature fluctuations during the synthesis or the lack of precision of the amount of OA consumed in the synthesis. As for the size characterization of UCNPs, TEM images are utilized as a complementary method and the measured mean size of UCNPs are indeed in close agreement with the tabulated results based on PM2K data analysis.

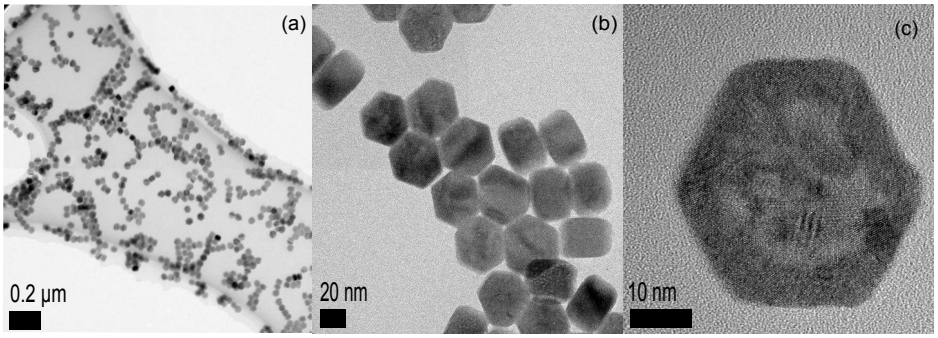

FIGURE 5.2: *TEM images of* $NaYF_4{:}Yb^{3+},Tm^{3+}$ *nanoparticles in sample core.*

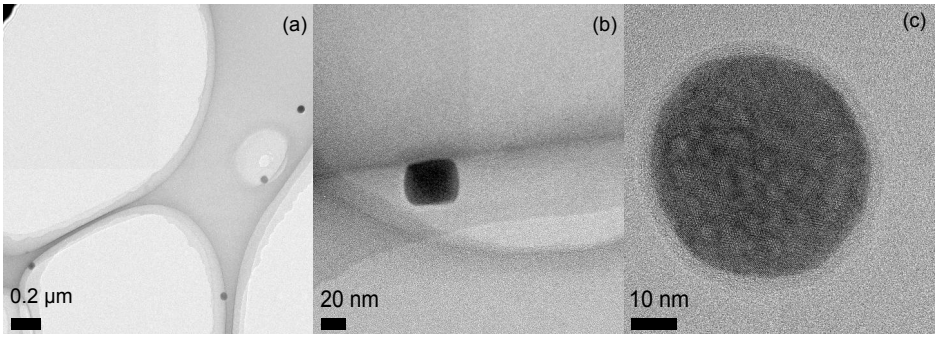

FIGURE 5.3: *TEM images of* $NaYF_4{:}Yb^{3+},Tm^{3+}@NaYF_4$ *nanoparticles in sample core-shell A.*

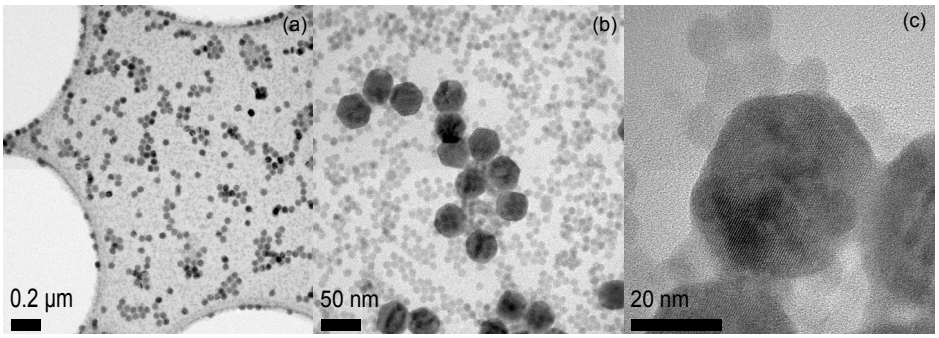

FIGURE 5.4: *TEM images of $NaYF_4$:Yb^{3+},Tm^{3+}@$NaYF_4$ nanoparticles in sample core-shell B.*

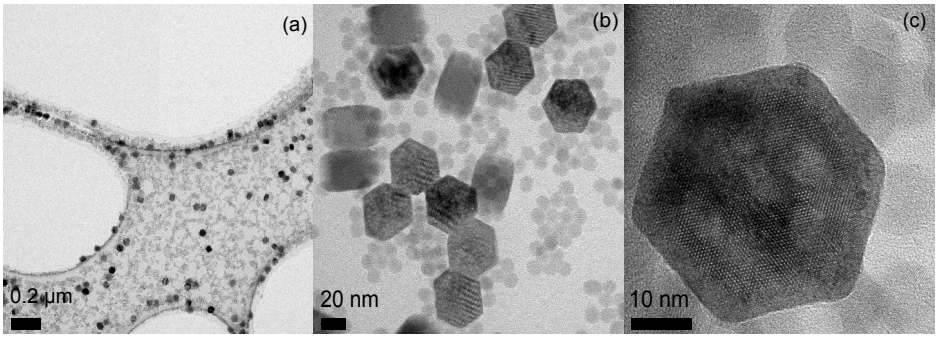

FIGURE 5.5: *TEM images of $NaYF_4$:Yb^{3+},Tm^{3+}@$NaYF_4$ nanoparticles in sample core-shell C.*

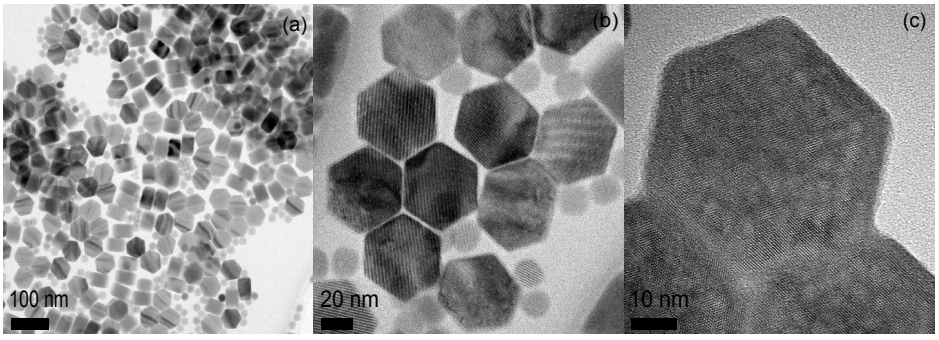

FIGURE 5.6: *TEM images of $NaYF_4$:Yb^{3+},Tm^{3+}@$NaYF_4$ nanoparticles in sample core-shell D.*

5.2 Thermal Stability Analysis on The Crystal Phase of Core and Core-Shell Upconverting Nanoparticles

Thermal stability investigation on the crystal phase of UCNPs at elevated temperature levels is carried out by a post-heating treatment based on an annealing process. UCNPs in core and core-shell A,B and C samples were heated gradually from room temperature to 700°C. As the annealing was carrying on, the XRD patterns of UCNPs at varying temperatures were obtained, presented in **Figures** 5.7, 5.8, 5.9 and 5.10.

The lowest temperature level for which an XRD pattern presented is 40°C for core sample and 60°C for samples A, B, C. With the exception of sample B, the very first XRD patterns for every other sample, marked in blue, are similar regardless of the intensity values. Similar to the previously presented XRD pattern of sample B at room temperature, the distinctive diffraction peak at **2θ=18°** in the XRD pattern of sample B is yet observed at relatively low temperature, 60°C, as expected. This implies that there is indeed more than one different crystal phase in sample B, which are cubic and hexagonal phases. For every sample, the XRD patterns are kept in blue colour in the **Figures** 5.7, 5.8, 5.9 and 5.10 until the very first change appears on the crystal phase due to the temperature.

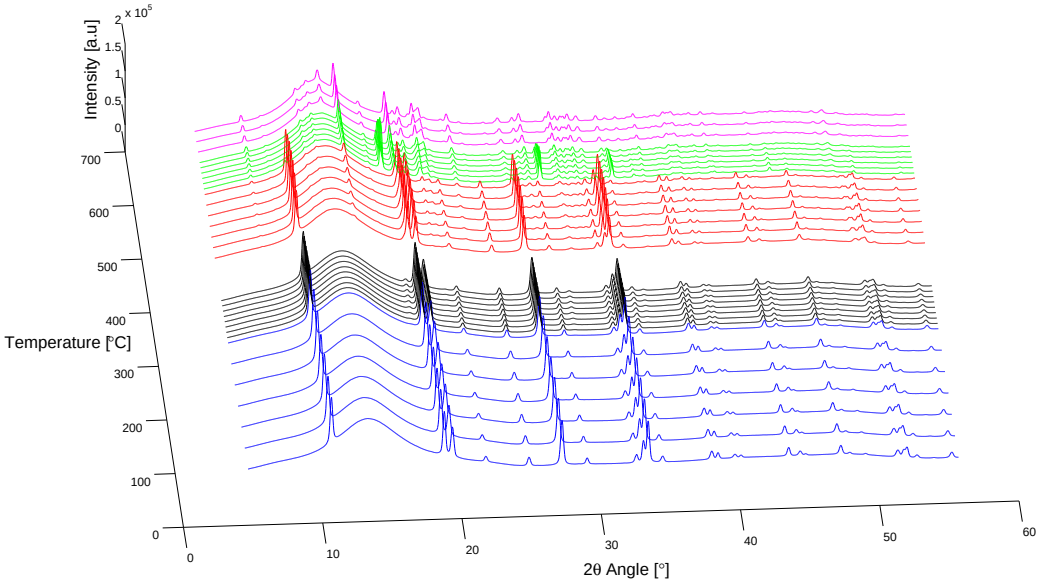

FIGURE 5.7: *The XRD patterns of the core UCNPs in sample core at varying temperatures. There is no change in the crystal phase of the nanoparticles till 310° C. A phase transformation represented by the XRD patterns coloured in green takes place between the temperatures of 590° C and 600° C.*

The corresponding XRD patterns of β-UCNPs in core sample shown in **Figure** 5.7 are thermally stable until the temperature reaches 310°C. New diffraction peaks indexed to the presence of relatively small sized α-NC residues, appear at 2θ angle of 18° and

30° and remain until temperature reads 460°C. At that level, the cubic crystal phase is exchanged with a new unknown crystal phase having a distinctive peak at 2θ angle of 15° represented by the XRD patterns in red colour. Thus, there are two different crystal phases, i.e., an unknown phase and an hexagonal phase at the temperatures between 460°C and 590°C. Remarkably, a phase transformation from the hexagonal phase to the cubic phase begins at 590°C and continues till 600°C, presented by the XRD patterns in green colour. The distinctive diffraction peaks indexed to the cubic crystal phase appear at 2θ angle of 18°, 29° and 34°. Subsequently, above 660°C the oxidation begins and deforms the core UCNPs. Thus, the unresolvable diffraction peaks emerge. On the other

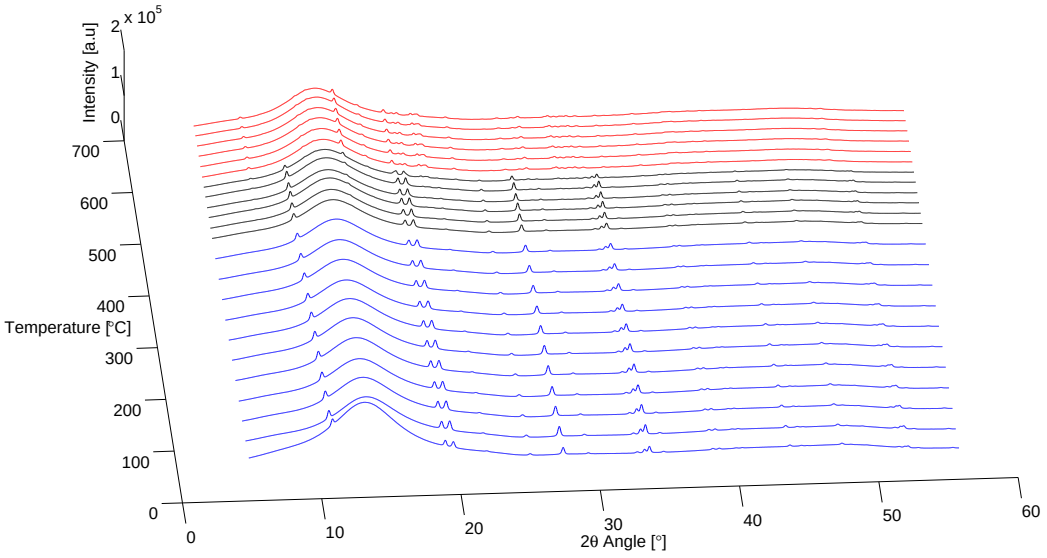

FIGURE 5.8: *The XRD patterns of the shell-coated UCNPs in sample A at varying temperatures. An unknown crystal phase with the corresponding diffraction peak at 2θ angle=15° appears at 480° C.*

hand, thermal stability of the shell-coated UCNPs in sample A shown in **Figure** 5.8 is higher than that of the core UCNPs. The very first change in the XRD pattern coloured in black is visible at 480°C with a diffraction peak at 2θ angle of 15° implying the presence of an unknown phase. Until 580°C, the unknown and the hexagonal phases are still observable. UCNPs do not undergo a phase transformation. The cubic crystal phase formation is not observed through the annealing. Above 600°C, the deformation of the particles starts. According to the XRD patterns shown in **Figure** 5.9, there are already two different crystal phases at room temperature. These are cubic and hexagonal phases. The majority of the β-UCNPs are thermally stable up to 520°C where an additional unknown phase is observed with a distinctive peak at 2θ angle of 15°. The temperatures between 590°C and 630°C, the XRD patterns with the diffraction peaks at 2θ angle of 18°, 29° and 34°, marked in green colour, imply that there is a phase transformation of UCNPs from the hexagonal crystal phase to the cubic crystal phase. Subsequently,

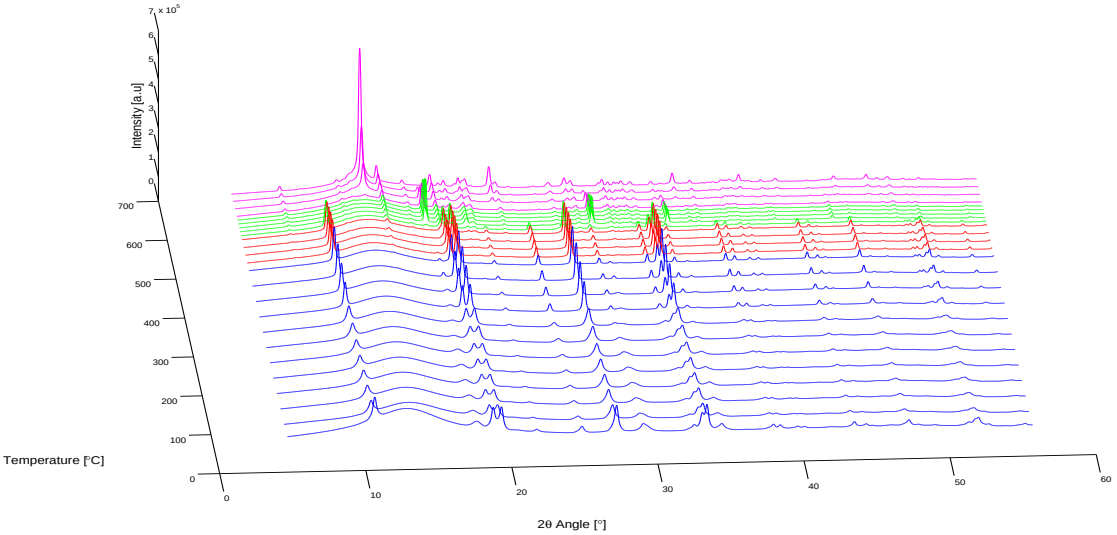

FIGURE 5.9: *The XRD patterns of the shell-coated UCNPs in sample B at varying temperatures. The nanoparticles are thermally stable till 520° C. UCNPs undergo a phase transformation represented by the XRD patterns coloured in green.*

above 630°C the diffraction peaks in the XRD patterns coloured in magenta could not be indexed to any known NC. For β-UCNPs in sample C, the thermal stability on the

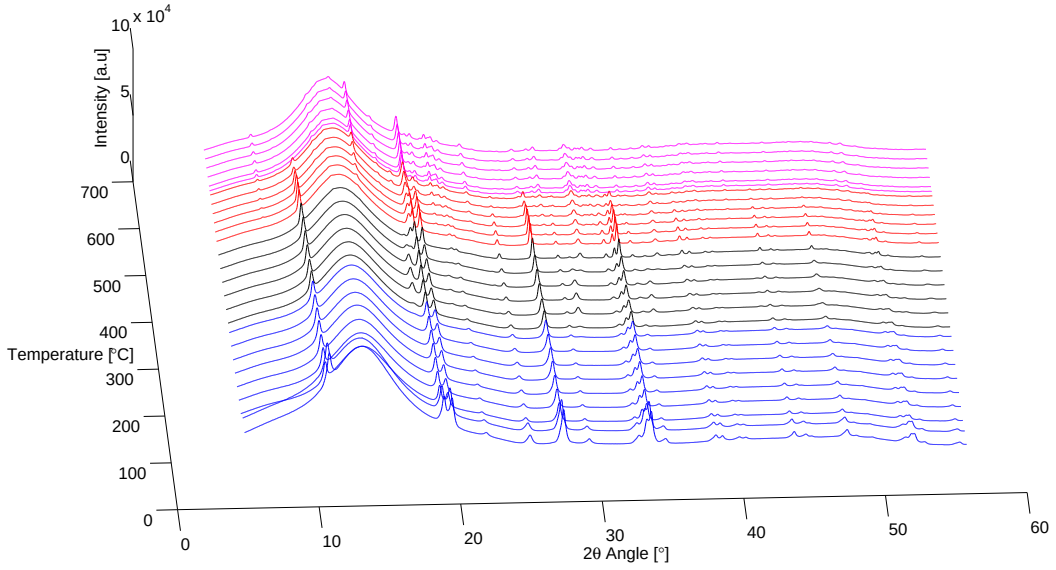

FIGURE 5.10: *The XRD patterns of the shell-coated UCNPs in sample C at varying temperatures. As from the temperature of 320° C, the crystal phase of UCNPs is no longer thermally stable.*

crystal phase is diminished around the temperature 320°C. The cubic crystal phase emerges having a diffraction peak at 2θ angle of 18° shown in the XRD patterns marked in black colour in **Figure** 5.10. The disappearance of the additional cubic phase at 510° is followed by the formation of an unknown phase having a distinctive diffraction peak at 2θ=15°. Subsequently, the inception point and the subsequent progress of the

oxidation yielding a deformation over NCs are represented by the XRD pattern coloured in magenta above 610°C.

5.3 Quantum Yield Enhancement in Core-Shell Upconverting Nanoparticles

The simulated and experimental results reveal a significant increase in the QY of NIR UC emission in core-shell $NaYF_4$:Yb^{3+},Tm^{3+}@$NaYF_4$ nanoparticles by exploiting millisecond pulsed excitation are presented in **Paper I**. The main results of that study will be outlined in this section.

For the QY measurements, the excitation source is set to be a CW laser diode at 975 nm (Thorlabs L975P1W). It is driven by a benchtop laser diode current controller (Thorlabs LDC220C) with the stabilized temperature at 25°C. The very same laser was employed to generate pulsed light output by modulating the current controller utilizing a function generator (Philips PM5139).

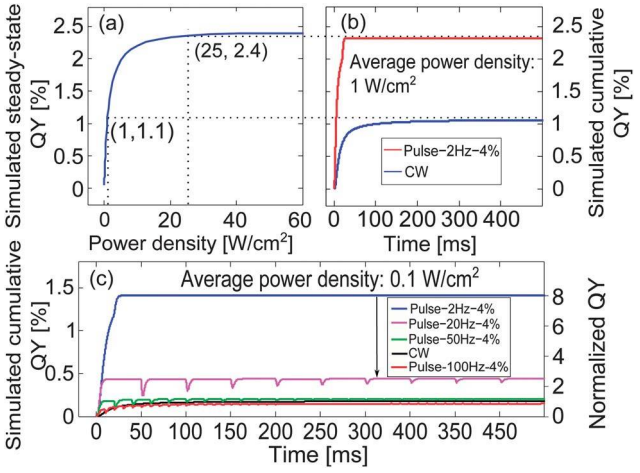

FIGURE 5.11: *(a) Simulated power density dependence of the QY in the NIR UC emission under CW excitation. (b) The cumulative QYs under CW excitation and under the pulsed excitation in the first pulse period. The average power density is 1 Wcm^{-2} for both excitation approaches. (c) The cumulative QYs under CW excitation and under the pulsed excitation in multiple periods. The average power density is 0.1 Wcm^{-2} for all excitation approaches.*

For the simulations, the rate equation technique presented in **Chapter 2** is used. This is described in detail in **Paper I**. Simulated cumulative QY_{pulsed} at the average power density of 1 Wcm^{-2} is ∼2.4 % in the end of the first pulse for the pulsed excitation with 2 Hz repetition rate and a 4% duty cycle, represented in **Figure** 5.11 **(b)**. The corresponding QY_{CW} is ∼1.1% measured under CW excitation with the same power density, shown in **Figure** 5.11 **(a)**. The pulsed excitation facilitates the late excitation photons to be utilized with higher energy conversion efficiency compared to the counterparts of the CW excitation. Therefore, the higher simulated cumulative QY is achieved

for the pulsed excitation with sufficient pulse widths. The simulated cumulative QY varies with the pulse widths. Thus, the pulsed excitation repetition rate is studied for 2 Hz, 20 Hz, 50 Hz and 100 Hz. Clearly seen in **Figure** 5.11 **(c)**, the simulated cumulative QY decreases with pulsed excitation with descending pulse width, i.e., higher repetition rate, which resulted in lower UC signal gain. In fact, at the point where the repetition rate is set to 100 Hz, the generated UC emission signal by CW excitation is slightly stronger than that generated by the pulsed excitation.

Herein, simulated results that disclose an increase in the QY in UCNPs are supported by the experimental results. The UC emission signal gain at 800 nm under excitation of 975 nm light was measured. Note that the UC signal gain is defined as $QY_{pulsed}/\ QY_{CW}$ in **Paper I**. The average power density of the pulsed excitation is adjusted to be ∼0.12 Wcm^{-2}, whilst it has a fixed duty cycle of 4 % alongside with different pulse widths. It is seen in **Figure** 5.12 **(a)** that the signal gain is measured to be ∼1.1 for 0.8 ms pulse width. The signal gain is ∼8.7 as the pulse width is tuned to be 20 ms. Clearly, the signal gain is increasing with increasing pulse width. At the point where signal gain is slightly higher than 1, the pulse width is remarkably shorter than 10 ms that is the approximated lifetime of the intermediate state $^3F_4$ of Tm^{3+} and thus the time required to generate the NIR UC emission.

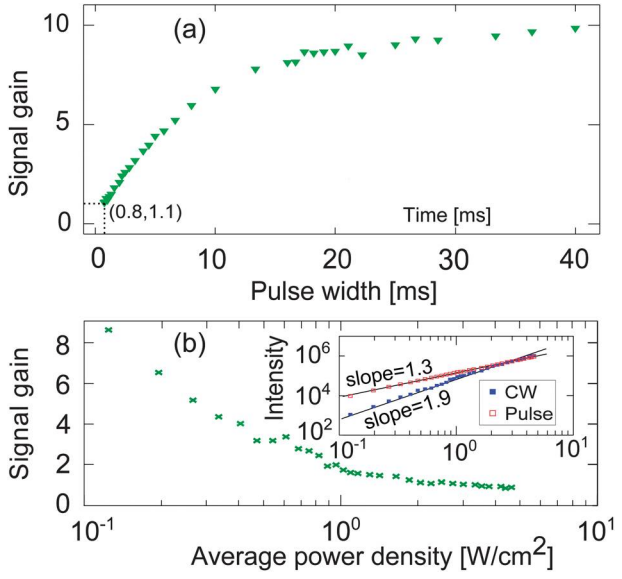

FIGURE 5.12: *(a) The NIR UC signal gain by the pulsed excitation with different pulse widths. (b) The average excitation power density dependence of the NIR UC signal gain by the pulsed excitation. The pulsed excitation was set to have a 20 ms pulse width and a 2 Hz repetition rate. Inset: The average excitation power density dependence of the NIR UC emission intensity under CW excitation and under the pulsed excitation.*

Moreover, the UC emission is dependent on applied excitation power density and this dependence is shown in **Figure** 5.12 **(b)**. A square-wave excitation with a 20 ms pulse and 2 Hz repetition rate is applied at varying average excitation power densities.

The UC signal gain of ∼8.7 is measured for lower power densities than ∼0.12 Wcm^{-2}. However, at the maximum excitation power density, ∼4.65 Wcm^{-2}, the UC signal gain declines to be less than 1. Although NIR UC emission gets more intense with higher power density of CW and pulsed excitations, the signal gain for the pulsed excitation would decrease. At the maximum level of excitation power density, the UC signal generated by CW is stronger than that of generated by the pulsed excitation. As a result of that, the UC signal gain is below 1 as the excitation power density is at maximum. The underlying reason is that UC emission intensity under pulsed excitation is not ascending in the same manner as that under CW excitation. The inset of **Figure** 5.12 **(b)** shows slopes of 1.3 and 1.9 for CW excitation and pulsed excitation, respectively. This clearly shows that the dependence of the emission intensity on the excitation power density differs for pulsed and CW excitations.

Chapter 6

Conclusion and Final Remarks

In this work, core $NaYF_4$:Yb^{3+},Tm^{3+} UCNPs and core-shell $NaYF_4$:Yb^{3+},Tm^{3+}@$NaYF_4$ UCNPs have been synthesized and characterized by different techniques, i.e. XRD, TEM and optical technique. Most of the synthesized UCNPs are in hexagonal shape and phase, ranging from 43 nm up to 66 nm in size at room temperature. Additionally, different shell covering the core particles have been successfully formed throughout the synthesis. In these synthesis steps, small amount of impurities with α- NCs in either rectangular or spherical shape and $\sim$1 nm in size were formed as observed in TEM images. The observed relatively high standard deviation in size is possibly due to temperature fluctuations during the synthesis. The temperature is one of the most significant experimental for UCNP synthesis. It controls the resulting crystal shape and size. Thus, a better temperature control with better instrumentation during the synthesis could be done for higher uniformity in particle size.

The very same UCNPs have been exposed to a post-heating treatment where the temperature level has been increased to 700°C. This was done to figure out the thermal stability of UCNPs' crystal phase. Core β-UCNPs show no change on the crystal phase observed until 310°C. Subsequently, the phase transformation from hexagonal to cubic is achieved at 590°C. In a similar manner, thermal stability of shell-coated UCNPs begins to degrade above 300°C. Additionally, above 600°C, all UNCPs, whether core or shell-coated, are being deformed due to the high oxidation. Since the intensity of the UC emission signal is highly dependent on the crystal phase of UCNPs, it has a significant importance to know at what level of temperature phase transformation occurs.

In addition, an enhancement of the NIR UC emission at around 800 nm in core-shell as compared to core is obtained under the excitation of 975 nm light. Experimental results therefore confirm a significant QY increase of the NIR UC emission using pulsed excitation with wisely selected pulse parameters at room temperature. Through the simulations, at $\sim$1 Wcm^{-2} of average excitation power density, the QY is increased to $\sim$ 2.4% from $\sim$ 1.1% as CW excitation is replaced by the pulsed excitation at a 2 Hz

repetition rate and a 4% duty cycle. Experimentally, the influence of pulse width on the UC signal gain at a constant power density is obtained. Longer pulse width results in higher signal gain. Thus, the UC signal gain increased from ∼1.1 to ∼8.7 by tuning the pulse width from 0.8 ms to 20 ms. It is worth mentioning that a 0.8 ms pulse width could be sufficient to accomplish a UC signal gain, despite the fact that it is a significantly shorter time than ∼10 ms, being the lifetime of the intermediate state $^3F_4$ of Tm^{3+}. Yet, it has been confirmed that the UC signal gain is excitation power density dependent. The UC signal gain has a tendency to decline with increasing excitation power density. The UC signal gain for the pulsed excitation is ∼8.7 at power density set to ∼0.12 Wcm^{-2} and subsequently becomes less than 1 as the excitation power density is increased to ∼4.65 Wcm^{-2}. Therefore, at maximum power density, the UC emission signal generated by pulsed excitation could become weaker than that generated by a corresponding CW excitation.

UCNPs are considered as promising contrast agents in diffuse optical imaging with their favorable characteristics. However, they suffer from a low QY of the UC emission at low fluence rates. This limits the possibility to reach plausible imaging depths. An increase in QY of the NIR UC emission could lead to a better image quality with higher imaging depths, as shown in **Paper I**. In particular, the signal gain at low excitation power densities is significant and would reduce the thermal side effects of the tissue due to excitation light.

Bibliography

[1] Leyu Wang, Ruoxue Yan, Ziyang Huo, Lun Wang, Jinghui Zeng, Jie Bao, Xun Wang, Qing Peng, and Yadong Li. Fluorescence resonant energy transfer biosensor based on upconversion-luminescent nanoparticles. *Angewandte Chemie International Edition*, 44(37):6054–6057, 2005. ISSN 1521-3773. doi: 10.1002/anie.200501907.

[2] H. Xing, W. Bu, H. Qu, Z. Wang, J. Shi, Q. Ren, X. Zheng, M. Li, Y. Hua, S. Zhang, K. Zhao, L. Zhou, and W. Peng. A naybf 4: Tm 3+ nanoprobe for ct and nir-to-nir fluorescent bimodal imaging. *Biomaterials*, 33(21):5384–5393, 2012. ISSN 01429612.

[3] Rufaihah A.J. Chatterjee, D.K. and Y. Zhang. Upconversion fluorescence imaging of cells and small animals using lanthanide doped nanocrystals. *Biomaterials*, 29: 937–943, 2008.

[4] Y. Chatterjee, D.K. & Zhang. Upconverting nanoparticles as nanotransducers for photodynamic therapy in cancer cells. *Nanomedicine*, 3:73–82, 2008.

[5] Guo H. Ho P. Mahendran R.and Zhang Y. Qian, H.S. Mesoporous silica coated up conversion fluorescent nanoparticles for photodynamic therapy. *Small*, 5:2285-2290, 2009.

[6] K.W. Krämer, D. Biner, G. Frei, H.U. Güdel, M.P. Hehlen, and S.R. Lüthi. Hexagonal sodium yttrium fluoride based green and blue emitting upconversion phosphors. *Chemistry of Materials*, 16(7):1244–1251, 2004. ISSN 08974756.

[7] J.F. Suyver, A. Aebischer, D. Biner, P. Gerner, J. Grimm, S. Heer, K.W. Kramer, C. Reinhard, and H.U. Gudel. Novel materials doped with trivalent lanthanides and transition metal ions showing near-infrared to visible photon upconversion. *Optical Materials*, 27(6):1111 – 1130, 2005.

[8] N. Bloembergen. Solid state infrared quantum counters. *Physical Review Letters*, 2(3):84–85, 1959. ISSN 00319007.

[9] V. V. Ovsyakin and P. P. Feofilov. Cooperative Sensitization of Luminescence in Crystals Activated with Rare Earth Ions. *ZhETF Pisma Redaktsiiu*, 4:471, December 1966.

[10] F. Auzel. Compteur quantique par transfert d energie entre deux ions de terres rares dans un tungstate mixte et dans un verre. *Comptes Rendus Hebdomadaires des Seances de L Academie des Sciences Serie B 262*, pages 1016–&, 1966.

[11] F. Auzel. Compteur quantique par transfert d energie de yb3+ and a tm3+ dans un tungstate mixte et dans un verre germanate. *Comptes Rendus Hebdomadaires des Seances de L Academie des Sciences Serie B 263,*, pages 819–&, 1966.

[12] F. Auzel. Upconversion and anti-stokes processes with f and d lons in solids. *Chemical Reviews*, 104(1):139 – 173, 2004. ISSN 00092665.

[13] F. Auzel. Multiphonon processes, cross-relaxation and upconversion in ion activated solids, exemplified by minilaser materials. *In Radiationless Processes, B. DiBartolo, V. Goldberg. Eds;Plenum Publishing Co. New York*, page 213, 1980.

[14] D. L. Dexter. A theory of sensitized luminescence in solids. *The Journal of Chemical Physics*, 21(5):836–850, 1953. doi: http://dx.doi.org/10.1063/1.1699044.

[15] R. Orbach. Optical properties of ions in solids. *B. DiBartolo, Ed; Plenum Press, New York*, page 445, 1975.

[16] M. Pollnau, D. R. Gamelin, S. R. Lüthi, H. U. Güdel, and M. P. Hehlen. Power dependence of upconversion luminescence in lanthanide and transition-metal-ion systems. *Phys. Rev. B*, 61:3337–3346, Feb 2000. doi: 10.1103/PhysRevB.61.3337.

[17] J. F. Suyver, A. Aebischer, S. García-Revilla, P. Gerner, and H. U. Güdel. Anomalous power dependence of sensitized upconversion luminescence. *Phys. Rev. B*, 71: 125123, Mar 2005. doi: 10.1103/PhysRevB.71.125123.

[18] F Wang and XG Liu. Recent advances in the chemistry of lanthanide-doped upconversion nanocrystals. *CHEMICAL SOCIETY REVIEWS*, 38(4):976 – 989, 2009. ISSN 03060012.

[19] M.F.H. Schuurmans and J.M.F. van Dijk. On radiative and non-radiative decay times in the weak coupling limit. *Physica B & C*, 123B+C(2):131 – 155, 1984.

[20] Zhang Y. Amalraj Appavoo I. Upconverting fluorescent nanoparticles for biological applications. *In Emerging Nanotechnologies for Manufacturing, Waqar A, Mark JJ, editors. Boston, MA: William Andrew*, pages 159–75, 2010.

[21] F. Zhang, J. Li, D. Zhao, J. Shan, and L. Xu. Shape, size, and phase-controlled rare-earth fluoride nanocrystals with optical up-conversion properties. *Chemistry - A European Journal*, 15(41):11010–11019, 2009. ISSN 09476539.

[22] J.F. Suyver, J. Grimm, M.K. Van Veen, D. Biner, K.W. Krämer, and H.U. Güdel. Upconversion spectroscopy and properties of nayf4 doped with er3+, tm3+ and/or yb3+. *Journal of Luminescence*, 117(1):1–12, 2006. ISSN 00222313.

[23] Zewei Quan, Dongmei Yang, Chunxia Li, Deyan Kong, Piaoping Yang, Ziyong Cheng, and Jun Lin. Multicolor tuning of manganese-doped zns colloidal nanocrystals. *Langmuir*, 25(17):10259–10262, 2009. doi: 10.1021/la901056d. PMID: 19705902.

[24] Guangshun Yi, Baoquan Sun, Fengzhen Yang, Depu Chen, Yuxiang Zhou, and Jing Cheng. Synthesis and characterization of high efficiency nanocrystal up conversion phosphors: Ytterbium and erbium codoped lanthanum molybdate. *Chemistry of Materials*, 14(7):2910–2914, 2002. doi: 10.1021/cm0115416.

[25] Amitava Patra, Christopher S. Friend, Rakesh Kapoor, and Paras N. Prasad. Upconversion in er3+:zro2 nanocrystals. *The Journal of Physical Chemistry B*, 106 (8):1909–1912, 2002. doi: 10.1021/jp013576z.

[26] Fiorenzo Vetrone, John-Christopher Boyer, John A. Capobianco, Adolfo Speghini, and Marco Bettinelli. Significance of yb3+ concentration on the upconversion mechanisms in codoped y2o3:er3+,yb3+ nanocrystals. *Journal of Applied Physics*, 96(1):661–667, 2004. doi: http://dx.doi.org/10.1063/1.1739523.

[27] Xiao Qin, Takeshi Yokomori, and Yiguang Ju. Flame synthesis and characterization of rare-earth (er3+, ho3+, and tm3+) doped upconversion nanophosphors. *Applied Physics Letters*, 90(7):073104, 2007. doi: http://dx.doi.org/10.1063/1.2561079.

[28] Y.-W. Zhang, X. Sun, R. Si, L.-P. You, and C. H. Yan. Single-crystalline and monodisperse laf3 triangular nanoplates from a single-source precursor. *Journal of the American Chemical Society*, 127(10):3260–3261, 2005. ISSN 00027863.

[29] J.C. Boyer, L.A. Cuccia, J.A. Capobianco, and F. Vetrone. Synthesis of colloidal upconverting nayf4 nanocrystals doped with er3+, yb3+ and tm3+, yb3+ via thermal decomposition of lanthanide trifluoroacetate precursors. *Journal of the American Chemical Society*, 128(23):7444–7445, 2006. ISSN 00027863.

[30] Hai-Sheng Qian and Yong Zhang. Synthesis of hexagonal-phase core-shell nayf4 nanocrystals with tunable upconversion fluorescence. *Langmuir*, 24(21):12123–12125, 2008. doi: 10.1021/la802343f.

[31] J. H. Zeng, J. Su, Z. H. Li, R.-X. Yan, and Y. D. Li. Synthesis and upconversion luminescence of hexagonal-phase nayf 4:yb, er3+ phosphors of controlled size and morphology. *Advanced Materials*, 17(17):2119–2123, 2005. ISSN 09359648.

[32] G. Yi, H. Lu, D. Chen, S. Zhao, Y. Ge, W. Yang, and L. H. Guo. Synthesis, characterization, and biological application of size-controlled nanocrystalline nayf4:yb,er infrared-to-visible up-conversion phosphors. *Nano Letters*, 4(11):2191–2196, 2004. ISSN 15306984.

[33] T. Sugimoto. Preparation of monodispersed colloidal particles. *Advances in Colloid and Interface Science*, 28(C):65–108, 1987. ISSN 00018686.

[34] Zhengquan Li and Yong Zhang. An efficient and user-friendly method for the synthesis of hexagonal-phase nayf 4 :yb, er/tm nanocrystals with controllable shape and upconversion fluorescence. *Nanotechnology*, 19(34):345606, 2008.

[35] Y. Wang, K. Liu, W.J. Buma, H. Zhang, X. Liu, X. Kong, M.C.G. Aalders, K. Dohnalová, and T. Gregorkiewicz. Critical shell thickness of core/shell upconversion luminescence nanoplatform for fret application. *Journal of Physical Chemistry Letters*, 2(17):2083–2088, 2011. ISSN 19487185.

[36] L. A. Svensson T. Ursby Å . Oskarsson J. Albertsson Y. Cerenius, K. Ståhl and A. Liljas. The crystallography beamline i711 at max ii,. *J. Synchrotron Rad,*, 7: 203–208, 2000.

[37] T. Confente M. Leoni and Z. Kristallogr. P. Scardi. Pm2k: a flexible program implementing whole powder pattern modelling. (23):249–254, 2006.

Paper I

Diffuse tissue optical imaging of upconverting nanoparticles enabled by exploiting higher intrinsic quantum yield through use of millisecond single pulse excitation with high peak power.

H. Liu, C. T. Xu, G. Dumlupinar, O. B. Jensen, P. E. Andersen, S. Andersson-Engels
Nanoscale 5, 10034-10040, 2013.

Nanoscale

RSC Publishing

PAPER

View Article Online
View Journal | View Issue

Cite this: *Nanoscale*, 2013, **5**, 10034

Deep tissue optical imaging of upconverting nanoparticles enabled by exploiting higher intrinsic quantum yield through use of millisecond single pulse excitation with high peak power†

Haichun Liu,*[a] Can T. Xu,[a] Gökhan Dumlupinar,[a] Ole B. Jensen,[b] Peter E. Andersen[b] and Stefan Andersson-Engels[a]

Received 17th April 2013
Accepted 22nd July 2013

DOI: 10.1039/c3nr01917a

www.rsc.org/nanoscale

We have accomplished deep tissue optical imaging of upconverting nanoparticles at 800 nm, using millisecond single pulse excitation with high peak power. This is achieved by carefully choosing the pulse parameters, derived from time-resolved rate-equation analysis, which result in higher intrinsic quantum yield that is utilized by upconverting nanoparticles for generating this near infrared upconversion emission. The pulsed excitation approach thus promises previously unreachable imaging depths and shorter data acquisition times compared with continuous wave excitation, while simultaneously keeping the possible thermal side-effects of the excitation light moderate. These key results facilitate means to break through the general shallow depth limit of upconverting-nanoparticle-based fluorescence techniques, necessary for a range of biomedical applications, including diffuse optical imaging, photodynamic therapy and remote activation of biomolecules in deep tissues.

1 Introduction

During the last decade, upconverting nanoparticles (UCNPs) have developed rapidly,[1–6] and show great promise as contrast agents in biological applications.[7–11] Despite tremendous improvements of UCNPs, their limited quantum yield (QY), especially at a low excitation light level, is still a major concern for most potential biological applications.[12] Two interesting and powerful techniques under development are deep tissue optical imaging[13] and photodynamic therapy (PDT),[14] both of which require high QY. The present low QY thus hinders the potential of these techniques to be unleashed due to prolonged data acquisition and treatment times, and shallow applicable depths.[12,15] Although low QY to some extent can be overcome by increasing the excitation light level, such improvements are fundamentally restricted for continuous wave (CW) excitation due to risks of tissue damage, regulated by the ANSI standards.[16]

Instead, the opportunity to break through the low power density limit of upconversion (UC) emission while limiting thermal effects of the excitation light is proposed here by employing pulsed excitation.[12,17,18] In addition, we realize that the applicability of UCNPs could be further boosted by utilizing single-shot excitation schemes, *i.e.*, short single pulse excitation with high peak power. Similar to multiphoton microscopy, pulsed excitation would provide high photon density during the pulse, while keeping the average power (*i.e.*, the deposited energy responsible for the heating) moderate. Due to the non-linear power density dependence of UC emission, pulsed excitation would be highly beneficial. However, two important differences exist between the UC emission and direct two-photon fluorescence. Firstly, the QY is much higher for UCNPs at low photon density rates, which constitutes one main reason for the interest in them and removes the reliance of and restriction to focal volume excitation, thus broadening their field of application.[19,20] Secondly, the excitation for UC emission relies on intermediate energy levels,[21] complicating the process. This has led to some less successful attempts to utilize pulsed excitation for UCNPs in the past.[22,23] It is thus necessary to carefully consider the excitation dynamics of UC emissions under pulsed excitation in order to utilize higher intrinsic QY of UCNPs.

In this paper, through investigation of the excitation dynamics of UC emission, we prove through simulations and experiments that significant QY increase can be achieved by using pulsed excitation with wisely selected pulse characteristics, *i.e.*, with sufficiently long pulse width and non-saturated energy transfer transitions. Our proposed scheme renders pulsed excitation an ideal excitation approach for UCNPs, especially for deeply located tissue volumes. In fact, the net QY

[a]*Department of Physics, Lund University, P.O. Box 118, S-221 00 Lund, Sweden. E-mail: haichun.liu@fysik.lth.se; Fax: +46 46 222 4250; Tel: +46 46 222 7471*

[b]*Department of Photonics Engineering, Technical University of Denmark, Frederiksborgvej 399, DK-4000 Roskilde, Denmark*

† Electronic supplementary information (ESI) available. See DOI: 10.1039/c3nr01917a

increase enables us to implement single-shot imaging of UCNPs, shortening data acquisition time by orders of magnitude while simultaneously improving imaging depth as compared to CW excitation. These results have the potential to fundamentally broaden the applicability of UCNPs in deep tissue regions relying on diffuse light excitation, breaking the shallow-depth limitation in UCNP-based imaging.

2 Experimental

2.1 Synthesis of UCNPs

Core–shell $NaYF_4$:Yb^{3+},Tm^{3+}@$NaYF_4$ nanoparticles, synthesized through a recently reported protocol,[24] are used as a representative of UCNPs in this work.

All the chemicals were purchased from Sigma-Aldrich and used without further purification. The core nanoparticles $NaYF_4$:Yb^{3+},Tm^{3+} were first synthesized using the protocol reported in ref. 25. In a typical synthesis, anhydrous powders of YCl_3 (0.75 mmol), $YbCl_3$ (0.25 mmol) and $TmCl_3$ (0.003 mmol) were dissolved in 6 mL oleic acid and 17 mL octadecene in a 250 mL flask at 160 °C for 30 min. After the clear solution cooled down to room temperature, 10 mL of a methanol solution containing 4 mmol NH_4F and 2.5 mmol NaOH was added, and the mixture was stirred for 30 min at 50 °C. The methanol was removed from the system by slowly heating it, and the resulting solution was heated to 300 °C for 1.5 h under argon atmosphere. After the mixture cooled to room temperature, the nanoparticles were precipitated with ethanol and washed with an ethanol–water mixture several times, and then redispersed in hexane to form a nanoparticle suspension. The core–shell nanoparticles were subsequently produced by slightly modifying the above procedure through incorporation of the prepared core nanoparticles as the seeds in the synthesis.[24] 1 mmol YCl_3 was solely used to provide rare-earth ions for the shielding layer. Other steps were kept the same as the synthesis of core nanoparticles.

2.2 Characterization and photoluminescence measurements on the UCNP suspension

The as-prepared core–shell UCNPs were dispersed in hexane and used as the sample. Transmission electron microscopy (TEM) images and the density of the UCNPs were measured on a JEOL 3000F microscope equipped with an X-ray energy dispersive spectroscopy (XEDS) facility. The molar concentrations of rare earth ions were measured on a PerkinElmer Optima 8300 inductively coupled plasma optical emission spectrometer (ICP-OES). The photoluminescence measurements were performed on a sensitive spectrometer setup. A CW laser diode at 975 nm (Thorlabs L975P1WJ) was employed as the excitation source driven by a benchtop laser diode current controller (Thorlabs LDC220C), with the temperature stabilized at 25 °C. Pulsed laser light output was achieved by modulating the current controller using a function generator (Philips PM5139). The excitation power was measured using an Ophir Nova II laser power meter equipped with a photodiode sensor (Ophir PD300), while the spot size of the excitation beam was measured using a laser beam profiler (DataRay Inc. WinCamD-UCD23). The emission light was detected using a grating spectrometer (Ocean Optics QE65000) with a slit width of 50 μm. The rise profile of the 800 nm emission was recorded by an oscilloscope (Tektronix TDS520A) coupled to the output of a photomultiplier tube (Hamamatsu R928), using excitation at 975 nm from a laser diode operating in the pulsed mode. All measurements were carried out at room temperature.

2.3 Diffuse optical imaging using UCNPs

Diffuse optical imaging of UCNPs in a liquid tissue phantom was performed either in *trans*-illumination or in *epi*-illumination mode. A capillary tube with an inner diameter of 2 mm, filled with a UCNP suspension, was immersed within the tissue phantom to simulate the luminescent target. Excitation of the UCNPs was accomplished either by a Thorlabs L975P1WJ laser diode running in the CW mode, or by a broad area laser (Eagleyard Photonics, EYP-BAL-0980-10000-4020-CDL02-0000) operating in the pulsed mode driven by a laser diode driver (LIMO LDD50). The excitation power was measured using an Ophir Nova II laser power meter equipped with a medium power thermal laser sensor [Ophir L40(150)A-SH-V2]. A charge-coupled device (CCD) camera (Andor iXon) was used to acquire fluorescence images.

3 Results and discussion

3.1 Numerical simulations on the QY increase by the pulsed excitation

The feasibility of increasing the QY of UCNPs using pulsed excitation is first investigated through numerical simulations. The Yb^{3+}/Tm^{3+} codoped nanoparticles are used as a representative of UCNPs in this work. The UC dynamics of their major UC emission band, *i.e.*, the NIR UC emission band at around 800 nm, is modeled using the following time-resolved rate equations based on its well verified UC pathway under excitation of 975 nm light,[21,29] as shown in Fig. 1,

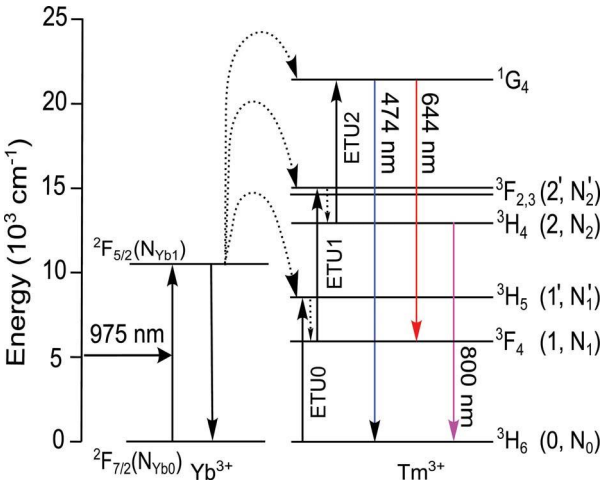

Fig. 1 Schematic energy level diagrams of Yb^{3+} and Tm^{3+} ions and the proposed UC mechanism following the excitation at 975 nm. The variables used in the text for the population densities of different levels are indicated within the parentheses.

$$\frac{dN_{Yb1}}{dt} = \frac{\sigma\rho}{h\nu}N_{Yb0} - (C_0N_0 + C_1N_1 + C_2N_2)\,N_{Yb1} - \frac{N_{Yb1}}{\tau_{Yb1}}, \quad (1a)$$

$$\frac{dN_1'}{dt} = C_0N_0N_{Yb1} - \beta_1'N_1', \quad (1b)$$

$$\frac{dN_1}{dt} = \beta_1'N_1' - C_1N_1N_{Yb1} - \frac{N_1}{\tau_1}, \quad (1c)$$

$$\frac{dN_2'}{dt} = C_1N_1N_{Yb1} - \beta_2'N_2', \quad (1d)$$

$$\frac{dN_2}{dt} = \beta_2'N_2' - C_2N_2N_{Yb1} - \frac{N_2}{\tau_2}, \quad (1e)$$

where σ is the absorption cross-section of Yb^{3+} ions; ρ is the excitation power density; h is Planck's constant; ν is the frequency of the excitation light; C_0, C_1 and C_2 are the energy transfer upconversion (ETU) rates from excited Yb^{3+} ions to the Tm^{3+} ions in states 0, 1 and 2, respectively; τ_1 and τ_2 are the radiative lifetimes of Tm^{3+} ions in states 1 and 2 (non-radiative de-excitation neglected for these levels), while τ_{Yb1} is the lifetime of Yb^{3+} ions in the $^2F_{5/2}$ state; β_1' and β_2' represent the non-radiative decay rates for $1' \rightsquigarrow 1$ and $2' \rightsquigarrow 2$, respectively. A power density dependent and temporally cumulative QY for the NIR UC emission in the time interval $[0, t]$, $\eta(\rho,t)$, is defined as

$$\eta(\rho,t) \equiv \frac{\int_0^t N_2(t)/\tau_2 dt}{\int_0^t \sigma N_{Yb0}\rho/h\nu dt}, \quad (2)$$

which can be calculated by numerically solving eqn (1a–e). The QY in the steady state following CW excitation is given by $\eta(\rho,\infty)$.

In the modeling, we used parameter values which were measured or calculated for the UCNPs used in the experimental work. The ion concentrations were calculated based on the TEM, ICP-OES and XEDS measurements on the UCNPs (see the ESI† for the calculation of ion concentrations), and the lifetimes τ_{Yb1} and τ_2 were measured experimentally. σ, τ_1, β_1' and β_2' were taken from the literature. The power density dependent steady-state QY of the used UCNPs has been measured and reported recently in our previous work.[30] The ETU rates were thus selected based on the principle of giving the best fitting of the simulated power density dependency of steady-state QY with the measured results (see the ESI† for the selection of the ETU rates). Table 1 summarizes the parameter values used in the simulations. Fig. 2a shows the simulated QY under steady-state conditions following CW excitation of different power densities. As seen, the QY increases with the excitation power density in a complex manner with a constant steady-state level (saturation level) at high power densities, which is consistent with experimental observations reported in the literature.[31,32]

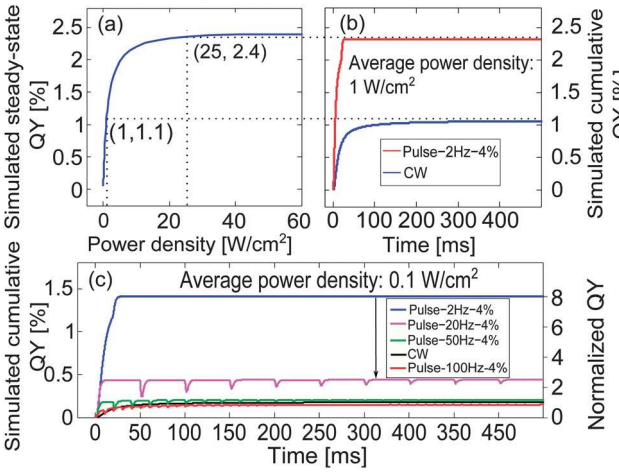

Fig. 2 (a) Simulated power density dependence of the QY of the NIR UC emission in the steady state under CW excitation. (b) The temporally cumulative QYs under CW excitation and under pulsed excitation in the first pulse period. The pulsed excitation had a duty cycle of 4% and a repetition rate of 2 Hz. Both the CW and pulsed excitation approaches provided an average power density of 1 W cm^{-2}. (c) The temporally cumulative QYs under CW excitation and under pulsed excitation in multiple periods. The pulsed excitation had a fixed duty cycle of 4% and various repetition rates. All the excitation approaches provided the same average power density of 0.1 W cm^{-2}.

Fig. 2b presents the simulated time dependent QY under CW excitation and under pulsed excitation in the first pulse period. The CW excitation has a constant power density of 1 W cm^{-2}. The pulsed excitation, having a 2 Hz repetition rate and a 4% duty cycle, has power densities of 25 W cm^{-2} and 0 W cm^{-2} in the "on" and "off" states, respectively, thus resulting in the same average power density as that of CW excitation. As shown in Fig. 2b, under CW excitation, the UC emission has a constant QY_{CW} except that at the very early stage when the energy levels start to be populated due to the effect of the excitation. This constant QY_{CW} is associated with the steady state of the UC system, and is given by the QY at the power density of 1 W cm^{-2} in Fig. 2a. Under pulsed excitation, the QY_{pulsed} is very small at the start of the laser pulse, and then increases with time. If the length of the pulse duration allows, the QY_{pulsed} will surpass the QY_{CW}, and asymptotically approach a maximum. This maximum is restricted to the steady-state QY at the power density of 25 W cm^{-2} in Fig. 2a. Clearly, the advantage of using pulsed excitation to replace the equivalent CW excitation is that the late excitation photons can be potentially used with higher energy conversion efficiency, while the disadvantage is that the

Table 1 Summary of general parameter values used in the simulations

σ (cm^2)	N_0 (cm^{-3})	N_{Yb0} (cm^{-3})	τ_{Yb1} (ms)	τ_1 (ms)	τ_2 (ms)	C_0 ($cm^3\ s^{-1}$)	C_1 ($cm^3\ s^{-1}$)	C_2 ($cm^3\ s^{-1}$)	β_1' (s^{-1})	β_2' (s^{-1})
1.69×10^{-20}[a]	1.25×10^{19}[b]	1.52×10^{21}[b]	1.32[c]	7.43[d]	1.49[c]	1.6×10^{-18}[e]	6.2×10^{-16}[e]	1.6×10^{-18}[e]	1.7×10^{4}[d]	1×10^{5}[d]

[a] From Jiang *et al.*[26] [b] Calculated (see the ESI† for the calculation of ion concentrations). [c] From measurement (see Fig. S2†). [d] From Ivanova *et al.*[27] [e] Estimated from Braud *et al.*[28] and Ivanova *et al.*[27] (see the ESI† for the selection of the ETU rates).

early excitation photons in each pulse period are used with lower efficiency than those in the CW excitation. Through balancing the increased power density and decreased excitation duration under the same amount of energy, an overall UC signal gain (defined as the ratio of the QY_{pulsed}/QY_{CW}) can be expected.

Cumulative QY in multiple periods under pulsed excitation was investigated in order to estimate the influence of the pulse width on the signal gain, compared to the equivalent CW excitation. The average power density was kept at 0.1 W cm^{-2} in the simulations. The pulsed excitation used throughout this study had the same duty cycle of 4% unless otherwise specified, and its repetition rate was adjusted in order to achieve different pulse widths. As illustrated in Fig. 2c, a significant UC signal gain is obtained by using pulsed excitation when the repetition rate is well below 50 Hz. For example, the signal gain by the 2 Hz square wave in the time interval of [0, 500] ms is approximately 8. The signal gain decreases with the repetition rate, *i.e.*, increases with pulse width as expected. When the repetition rate is even higher, *e.g.*, up to 100 Hz, the signal generated by the pulsed excitation becomes slightly smaller than that generated by equivalent CW excitation. In addition, it should be noted that the signal gain decreases with the applied power density. When the average power density is increased to 1 W cm^{-2}, the signal gain decreases to 2, as shown in Fig. S3.† This can be ascribed to the gradual saturation property of UC emission, indicated in Fig. 2a.

Although the parameter values were carefully calculated or modified in the simulations so that they gave the best fitting between the measured and simulated steady-state QY power density dependency, the modeling is not an accurate description of the real UC system. Due to the lack of accuracy and precision data for such values, it is difficult to evaluate the uncertainty of the simulated results. However, the influence of the variation of parameter values on the simulated signal gain was investigated, with the results for the change of ETU rates shown in Fig. S4.† In each comparison, one ETU rate among others was adjusted across the two orders of magnitude around the value listed in Table 1, while two other ETU rates remained unchanged. All simulated results confirm that the UC emission enhancement effect can be achieved by using pulsed excitation with a considerably long pulse duration when the energy transfer transitions are not saturated by the applied power density, as long as the emission originates from a multi-stepwise photon upconversion process. The only difference exists in the extent of the signal gain. It is worth mentioning that the simulated signal gain has a strong dependence on the change of the ETU rate C_1 rather than C_0 and C_2, as shown in Fig. S4.† This can be explained by the fact that the balancing power density of UCNPs is highly dependent on C_1.[30] Above this power density, the UCNPs would behave more linearly in emitting upconverted photons upon NIR excitation,[30] leading to decreased signal gain by using pulsed excitation.

3.2 Quantum yield increase by pulsed excitation in the UCNP suspension

In order to experimentally validate the gain in the UC signal due to the pulsed excitation predicted by the simulations in Section 3.1, experiments were carried out on colloidal stable UCNPs.

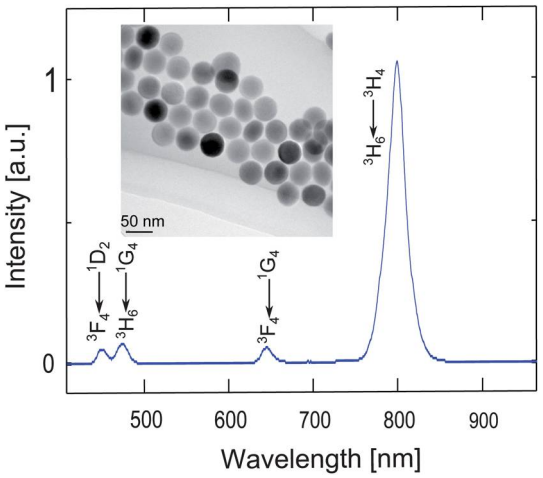

Fig. 3 The upconversion spectrum of core–shell $NaYF_4$:Yb^{3+},Tm^{3+}@$NaYF_4$ nanoparticles under excitation of a CW 975 nm laser diode, measured at a power density of 125 W cm^{-2}. The inset shows the TEM image of the prepared core–shell UCNPs.

Core–shell $NaYF_4$:Yb^{3+},Tm^{3+}@$NaYF_4$ UCNPs were dispersed in hexane and used as the sample. The prepared UCNPs emit the major UC emission bands at around 800 nm under excitation of 975 nm light, as shown in Fig. 3, assigned to the transition $^3H_4 \rightarrow {}^3H_6$ of Tm^{3+} ions.[29] Other weaker UC emission bands at around 450 nm, 474 nm and 644 nm originate from the transitions of Tm^{3+} ions: $^1D_2 \rightarrow {}^3F_4$, $^1G_4 \rightarrow {}^3H_6$ and $^1G_4 \rightarrow {}^3F_4$, respectively.[29] The inset of Fig. 3 shows the TEM image of the prepared core–shell UCNPs. The nanoparticles were spherical in shape with an average diameter of 42 nm. The core nanoparticles prior to coating had an average diameter of 32 nm (see Fig. S1 in the ESI†).

The intensities of the NIR UC emission under CW excitation and pulsed excitation (square wave) were measured. The pulsed excitation had a fixed duty cycle of 4% and different pulse widths. The average power density of the excitation light was kept at 0.12 W cm^{-2}. As shown in Fig. 4a, a signal gain, monotonically increasing with pulse width, was obtained by using the pulsed excitation even with a pulse duration as short as 0.8 ms. When the pulse width reaches 20 ms, the gain is as high as 8.7. It is noteworthy to point out that the required pulse width for the UC signal gain in the present case (~0.8 ms) is much shorter than the rise time of the UC emission (*i.e.*, approximately 10 ms, as shown in the inset of Fig. 4a), dominated by the lifetime of the intermediate level $^3F_4$ of Tm^{3+} ions. This is different from previous predictions reported in the literature,[12,18] and makes the pulsed excitation approach even more flexible to use due to a broader pulse width window for QY increase.

The dependence of the gain in the UC signal on the applied power density was also investigated using a square-wave excitation with a 20 ms pulse width and 2 Hz repetition rate. Fig. 4b shows the UC signal gain by the pulsed excitation at various average excitation power densities, where a decreasing trend with increasing excitation power densities is clearly seen. At the minimum power density investigated (~0.12 W cm^{-2}), the

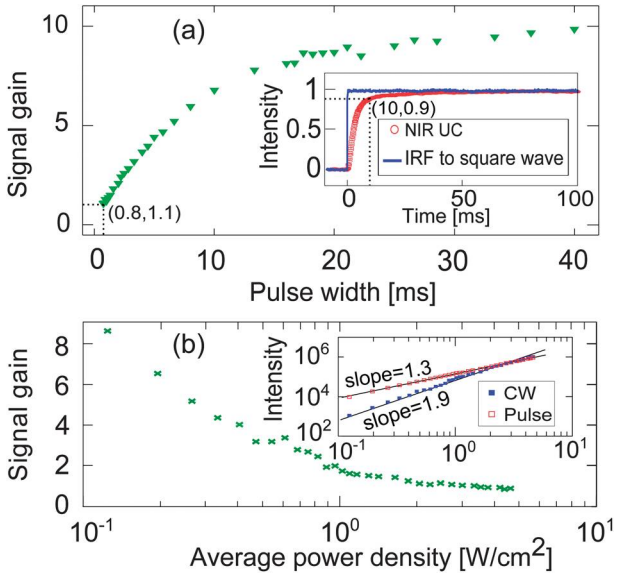

Fig. 4 (a) The NIR UC signal gain by the pulsed excitation with different pulse widths. The data were measured with an average excitation power density of 0.12 W cm^{-2}. Inset: the response of the NIR UC emission to a square-wave excitation with IRF denoting the instrument response function. (b) The dependence of the NIR UC signal gain by the pulsed excitation on the average power density. The pulsed excitation was set to have a 20 ms pulse width and 2 Hz repetition rate. Inset: the average power density dependence of the NIR UC emission intensity under CW and pulsed excitations.

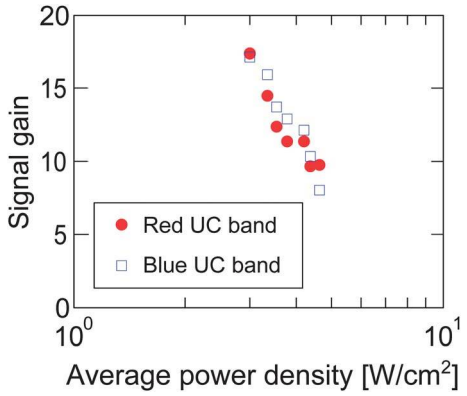

Fig. 5 The dependency of the blue (at 474 nm) and red (at 644 nm) UC signal gains by the pulsed excitation on the average power density. The pulsed excitation was set to have a pulse width of 20 ms and a repetition rate of 2 Hz.

signal gain is approximately 8.7, while at the maximum power density (~4.65 W cm^{-2}), the UC signal generated by the pulsed excitation is slightly weaker than that generated by the CW excitation. The UC emission intensity dependence on the excitation power density under pulsed excitation exhibits a smaller slope than that under the CW excitation, as shown in the inset of Fig. 4b, which could explain the signal-gain trend above.

The amplification effect of increasing the excitation power density here essentially originates from the non-linear power density dependence of the UC emission. Thus, a higher-order power density dependence would result in a larger UC signal gain. This is confirmed by the measurements on the blue (at 474 nm) and red (at 644 nm) UC emissions, both generated through a three-photon excitation process. They exhibit significantly larger signal gains than the NIR UC emission at any given average power density, as shown in Fig. 5. In view of this, we foresee that pulsed excitation can be employed to increase the applicability of recently implemented migration-mediated UC emissions from ions such as Eu^{3+} and Tb^{3+} in biological applications, due to their high-order multi-stepwise excitation nature *via* excited Tm^{3+} ions.[33] At present, their applications in such areas are challenged due to their low QYs.

It is worth mentioning that the usefulness of pulsed excitation for increasing the QY of UC emissions is not merely limited to Yb^{3+}/Tm^{3+} codoped UCNPs. Instead, it is a general scheme for enhancing UC emissions and would work in diverse UCNPs with different dopants if the characteristic of the pulsed excitation light is wisely tailored. In addition, as different UCNPs exhibit different optical characteristics, proper characterization will make it possible to accurately predict the performance of UCNPs in general under pulsed excitation.

3.3 Single-shot imaging of UCNPs

When UCNPs are used as contrast agents in diffuse optical imaging, the imaging depth is usually shallow due to the very low QY of UC emissions at the low fluence rates found in deep tissues.[12] The pulsed excitation constitutes an ideal approach for exciting deeply located UCNPs, since the UC emissions can be enhanced without consuming more excitation energy than an equivalent CW source, thus not increasing the thermal side-effects of the excitation light. This would in turn lead to higher image quality and larger imaging depth.

The merit of using pulsed excitation light to image deeply located UCNPs was subsequently tested in a liquid tissue phantom. The phantom, made of water, intralipid and ink, was characterized by photon time-of-flight spectroscopy (pTOFS)[34] and determined to have reduced scattering coefficient $\mu_s' = 10.1\ cm^{-1}$ and absorption coefficient $\mu_a = 0.52\ cm^{-1}$ at 975 nm, hence mimicking skin tissue properties. Its thickness was 17 mm. A glass tube with an inner diameter of 2 mm, containing the colloidal core–shell UCNPs ($c = 1$ wt%), was inserted into the phantom as the luminescent inclusion to mimic a UCNP-labeled target, *e.g.*, a tumor inside real tissue. CW excitation and pulsed excitation, having 20 ms pulse duration and 2 Hz repetition rate, at 975 nm were applied, respectively. The average power density impinging on the surface of the tissue phantom was 1.2 W cm^{-2} for both excitation approaches. The excitation source and the detector were positioned in a *trans*-illumination geometry. A more detailed description of the experimental setup is found in ref. 32. When buried at a depth of 10 mm from the source, the luminescent inclusion was barely detectable under CW excitation even with an exposure time of 10 s, as shown in Fig. 6a. However, by using pulsed excitation, the signal-to-background ratio was significantly increased by a factor of approximately 7 under the same detection conditions, as illustrated in Fig. 6b. An obvious implication is that the data acquisition time can be drastically reduced whilst maintaining the signal quality equivalent to CW excitation. Moreover, it is

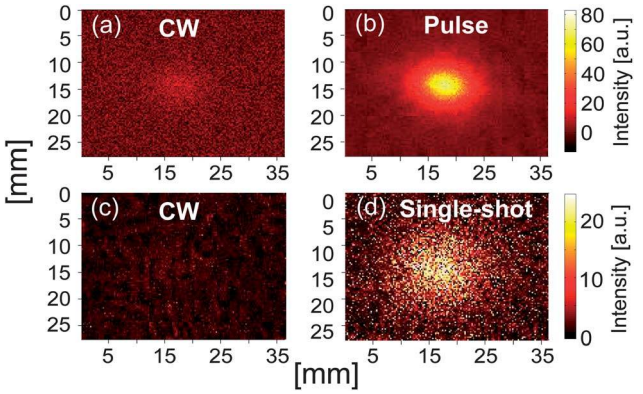

Fig. 6 The NIR UC emission images taken for a luminescent inclusion located at a depth of 10 mm under the (a) CW and (b) pulsed excitation, detected in a *trans*-illumination geometry. The average power density was 1.2 W cm^{-2}, and the exposure time was 10 s for both excitation approaches. The NIR UC emission images taken for a luminescent inclusion located at a depth of 13 mm under the (c) CW and (d) 50 ms single pulse excitation, detected in an *epi*-illumination geometry. Both excitation sources provided the maximum permissible power density allowed by the ANSI standard for exposure to human skin. The exposure time was 10 s for the CW excitation and 1 s for the single pulse excitation.

notable that the maximum imaging depth can be increased to 15 mm for pulsed excitation (data not shown).

The QY of UC emission can be further optimized by using single pulse excitation, through which even higher power density can be achieved. For instance, the maximum permissible power density for exposure to human skin at 975 nm is 17.4 W cm^{-2} for a repetitive pulse excitation with a pulse width of 20 ms and a repetition rate of 2 Hz, while the number for a 50 ms single pulse is as high as 36.9 W cm^{-2},[16] referring to Section 8 in the ESI.† Such a strong single pulse with a pulse width longer than the rise time of the UC emission enables the UCNPs to be used in a very efficient way in terms of energy conversion. This excitation approach would improve the imaging ability of using UCNPs without violating the ANSI standard, which is a fundamental limit for bio-imaging.

The feasibility of single-shot imaging was experimentally investigated. A 50 ms single pulse providing an excitation power density of 36.9 W cm^{-2} was used. When the luminescent inclusion was placed at a depth of 13 mm into the phantom, it could be relatively well detected using the single pulse excitation with a detector integration time of 1 s, even using an *epi*-illumination imaging setup described in ref. 17, as shown in Fig. 6d. Nevertheless, when the CW laser was used for excitation, also outputting the maximum permissible power density by the ANSI standard on the same illumination area, *i.e.*, 709.6 mW cm^{-2}, referring to Section 8 in the ESI,† the inclusion was not detectable at all even with a much longer integration time of 10 s, as shown in Fig. 6c. Obviously, the integration time for the single pulse excitation can be shortened to 50 ms still without loss in the UC signal quality, as long as the excitation source and the detector are synchronized. The results demonstrated here, although preliminary, show great potential of single-shot excitation in UCNP-guided deep tissue optical imaging.

4 Conclusions

In conclusion, significant QY increase in UCNPs is achieved by using pulsed excitation. This is supported theoretically by the study of the UC dynamics based on time resolved rate equations. Such QY increase enables us to implement single-shot imaging of UCNPs in deep tissues. Pulsed excitation thus constitutes an ideal excitation approach for UCNPs, as the shallow imaging limit can be overcome and data acquisition time can be drastically shortened by applying this excitation scheme. The pulsed excitation approach will greatly increase the applicability of UCNPs not only in diffuse optical imaging but also in many other biomedical applications, such as photodynamic therapy and remote activation of biomolecules in deep tissues.[35,36] It is worth mentioning that metallic nanostructures are reported to be effective in enhancing UC emissions owing to their local field enhancement effect by surface plasmonic coupling.[37] We envisage that the combination of the pulsed excitation approach and metallic nanostructures could become a major scheme of using UCNPs in the diffuse light regime, due to the synergistic effect in increasing the excitation power density. In addition, this study provides a general method for promoting the applications of nonlinear fluorophores (including UCNPs and triplet–triplet annihilation based upconverters[38]) under low light conditions by increasing the excitation fluence rate through a limited illumination area.

Acknowledgements

S. Fredriksson, F. Olsson, A. Gisselsson, and P. Kjellman are gratefully acknowledged for the help with the synthesis of the UCNPs and ICP-OES measurement. M. E. Messing and L. R. Wallenberg are acknowledged for the help with the TEM and XEDS measurements. B. Thomasson is acknowledged for the help in the single-shot imaging experiment. S. Johansson and A. Shaharin are acknowledged for the help with the pTOFS measurements. We thank D. Kroon and D. Guenot for the assistance in the laser power measurement, and J. Axelsson and P. Svenmarker for their helpful discussions. This work was supported by a grant from the Swedish Research Council (grant no. 621-2011-4265) and a Linneaus grant to the Lund Laser Centre.

References

1 X. Wang, J. Zhuang, Q. Peng and Y. D. Li, *Nature*, 2005, **437**, 121–124.
2 H.-X. Mai, Y.-W. Zhang, R. Si, Z.-G. Yan, L.-D. Sun, L.-P. You and C.-H. Yan, *J. Am. Chem. Soc.*, 2006, **128**, 6426–6436.
3 J.-C. Boyer, L. A. Cuccia and J. A. Capobianco, *Nano Lett.*, 2007, **7**, 847–852.
4 E. M. Chan, C. Xu, A. W. Mao, G. Han, J. S. Owen, B. E. Cohen and D. J. Milliron, *Nano Lett.*, 2010, **10**, 1874–1885.
5 F. Wang, Y. Han, C. S. Lim, Y. Lu, J. Wang, J. Xu, H. Chen, C. Zhang, M. Hong and X. Liu, *Nature*, 2010, **463**, 1061–1065.
6 F. Zhang, G. B. Braun, A. Pallaoro, Y. Zhang, Y. Shi, D. Cui, M. Moskovits, D. Zhao and G. D. Stucky, *Nano Lett.*, 2012, **12**, 61–67.

7 L. Wang, R. Yan, Z. Huo, L. Wang, J. Zeng, J. Bao, X. Wang, Q. Peng and Y. Li, *Angew. Chem., Int. Ed.*, 2005, **44**, 6054–6057.
8 S. F. Lim, R. Riehn, W. S. Ryu, N. Khanarian, C. K. Tung, D. Tank and R. H. Austin, *Nano Lett.*, 2006, **6**, 169–174.
9 M. Nyk, R. Kumar, T. Y. Ohulchanskyy, E. J. Bergey and P. N. Prasad, *Nano Lett.*, 2008, **8**, 3834–3838.
10 H. Päkkilä, M. Ylihärsilä, S. Lahtinen, L. Hattara, N. Salminen, R. Arppe, M. Lastusaari, P. Saviranta and T. Soukka, *Anal. Chem.*, 2012, **84**, 8628–8634.
11 M. Yu, F. Li, Z. Chen, H. Hu, C. Zhan, H. Yang and C. Huang, *Anal. Chem.*, 2009, **81**, 930–935.
12 C. T. Xu, Q. Zhan, H. Liu, G. Somesfalean, J. Qian, S. He and S. Andersson-Engels, *Laser Photonics Rev.*, 2012, DOI: 10.1002/lpor201200052.
13 J. Zhou, Z. Liu and F. Li, *Chem. Soc. Rev.*, 2012, **41**, 1323–1349.
14 N. M. Idris, M. K. Gnanasammandhan, J. Zhang, P. C. Ho, R. Mahendran and Y. Zhang, *Nat. Med.*, 2012, **18**, 1580–1585.
15 F. C. J. M. van Veggel, C. Dong, N. J. J. Johnson and J. Pichaandi, *Nanoscale*, 2012, **4**, 7309–7321.
16 Laser Institute of America, *Americal National Standard for Safe Use of Lasers; in ANSI Z136.1-2000*, Laser Institute of America, Orlando, Florida, 2000.
17 C. T. Xu, N. Svensson, J. Axelsson, P. Svenmarker, G. Somesfalean, G. Chen, H. Liang, H. Liu, Z. Zhang and S. Andersson-Engels, *Appl. Phys. Lett.*, 2008, **93**, 171103.
18 Q. Zhan, S. He, J. Qian, H. Cheng and F. Cai, *Theranostics*, 2013, **3**, 303–316.
19 H. Liu, C. T. Xu and S. Andersson-Engels, *Opt. Lett.*, 2010, **35**, 718–720.
20 P. Svenmarker, C. T. Xu and S. Andersson-Engels, *Opt. Lett.*, 2010, **35**, 2789–2791.
21 F. Auzel, *Chem. Rev.*, 2004, **104**, 139–173.
22 L. M. Maestro, E. M. Rodriguez, F. Vetrone, R. Naccache, H. L. Ramirez, D. Jaque, J. A. Capobianco and J. G. Solé, *Opt. Express*, 2010, **18**, 23544–23553.
23 C. F. Gainer, G. S. Joshua, C. R. De Silva and M. Romanowski, *J. Mater. Chem.*, 2011, **21**, 18530–18533.
24 H.-S. Qian and Y. Zhang, *Langmuir*, 2008, **24**, 12123–12125.
25 Z. Li and Y. Zhang, *Nanotechnology*, 2008, **19**, 345606.
26 X. P. Jiang, Z. M. Yang, T. Liu and S. H. Xu, *J. Appl. Phys.*, 2009, **105**, 103113.
27 S. E. Ivanova, A. M. Tkachuk, A. Mirzaeva and F. Pelle, *Opt. Spectrosc.*, 2008, **105**, 228–241.
28 A. Braud, S. Girard, J. L. Doualan, M. Thuau, R. Moncorg'e and A. M. Tkachuk, *Phys. Rev. B: Condens. Matter Mater. Phys.*, 2000, **61**, 5280–5292.
29 G. Chen, T. Y. Ohulchanskyy, R. Kumar, H. Ågren and P. N. Prasad, *ACS Nano*, 2010, **4**, 3163–3168.
30 H. Liu, C. T. Xu, D. Lindgren, H. Xie, D. Thomas, C. Gundlach and S. Andersson-Engels, *Nanoscale*, 2013, **5**, 4770–4775.
31 R. Page, K. Schaffers, P. Waide, J. Tassano, S. Payne, W. Krupke and W. Bischel, *J. Opt. Soc. Am. B*, 1998, **15**, 996–1008.
32 C. T. Xu, P. Svenmarker, H. Liu, X. Wu, M. E. Messing, L. R. Wallenberg and S. Andersson-Engels, *ACS Nano*, 2012, **6**, 4788–4795.
33 F. Wang, R. Deng, J. Wang, Q. Wang, Y. Han, H. Zhu, X. Chen and X. Liu, *Nat. Mater.*, 2011, **10**, 968–973.
34 T. Svensson, E. Alerstam, D. Khoptyar, J. Johansson, S. Folestad and S. Andersson-Engels, *Rev. Sci. Instrum.*, 2009, **80**, 063105.
35 C. J. Carling, F. Nourmohammadian, J. C. Boyer and N. R. Branda, *Angew. Chem., Int. Ed.*, 2010, **49**, 3782–3785.
36 M. K. G. Jayakumar, N. M. Idris and Y. Zhang, *Proc. Natl. Acad. Sci. U. S. A.*, 2012, DOI: 10.1073/pnas.1114551109.
37 S. Schietinger, T. Aichele, H.-Q. Wang, T. Nann and O. Benson, *Nano Lett.*, 2010, **10**, 134–139.
38 S. Baluschev, T. Miteva, V. Yakutkin, G. Nelles, A. Yasuda and G. Wegner, *Phys. Rev. Lett.*, 2006, **97**, 143903.

